

₁ Physics-Infused Reduced-Order Modeling for Analysis of
₂ Ablating Hypersonic Thermal Protection Systems

₃

₄

November 16, 2025

₅

Abstract

₆

This work presents a *physics-infused reduced-order modeling* (PIROM) framework towards the design, analysis, and optimization of non-decomposing ablating hypersonic thermal protection systems (TPS). It is demonstrated via the modeling of transient thermo-ablative behavior of non-decomposing multi-layered hypersonic TPS. The PIROM architecture integrates a reduced-physics backbone, based on the lumped-capacitance model (LCM), with data-driven correction dynamics formulated via a coarse-graining approach rooted in the Mori-Zwanzig formalism. The LCM is coupled to a surface velocity model (SVM) to capture the recession of the ablating TPS as a function of the surface temperature. While the LCM and SVM capture the dominant physics of the ablating TPS response, the correction terms compensate for residual dynamics arising from higher-order non-linear interactions and heterogeneities across material layers. The PIROM consistently achieves errors below 1% for a wide range of extrapolative settings of design parameters involving time-and-space varying boundary conditions and SVM models, and improves by $x\%$ over the LCM alone. Moreover, the PIROM delivers online evaluations that are two orders of magnitude faster than the full-order model (FOM). These results demonstrate that PIRO effectively reconciles the trade-offs between accuracy, generalizability, and efficiency, providing a promising

23 framework for optimizing multi-physical dynamical systems, such as TPS under diverse
24 operating conditions.

25 1 Introduction

26 At hypersonic speeds, aerospace vehicles experience extreme aero-thermo-dynamic environ-
27 ments that require specialized thermal protection systems (TPS) to shield internal sub-
28 structures, electronics, and possibly crew members from the intense aerodynamic heating.
29 The TPS is often composed of ablating materials – a high-temperature capable fibrous
30 material injected with a resin that fills the pore network and strengthens the compos-
31 ite [Amar2016](#). The TPS design promotes the exchange of mass through thermal and
32 chemical reactions (i.e., pyrolysis), effectively mitigating heat transfer to the sub-structures.

33 As a result, accurate prediction for the ablating TPS response under extreme hyper-
34 sonic heating becomes fundamental to ensuring survivability, performance, and safety of
35 hypersonic vehicles. Not only is it necessary to assess the performance of the thermal man-
36 agement systems, but also the shape changes of the vehicle’s outer surface induced by the
37 ablating material, and its impact on the aerodynamics, structural integrity, and controlla-
38 bility. Nonetheless, high-fidelity simulations of ablating TPS remains a formidable challenge
39 both theoretically and computationally.

40 Unfortunately, high-fidelity simulations of ablating TPS remains a formidable challenge
41 both theoretically and computationally.

42 On the theoretical side, the thermo-chemical reactions, coupled with the irregular pore
43 network structure, translate into simplifying assumptions to reduce non-linearities, and make
44 the resulting equations more amenable for engineering application and design analysis [x](#).
45 For instance, one of the most notable codes is the one-dimensional [CMA](#) code that was
46 developed by Aerotherm Corporation in the 1960s [Howard2015](#). Despite its practical use
47 in...

48 Another example is the CHarring Ablator Response (CHAR) ablation code, which ignores
49 elemental decompositions of the pyrolyzing gases, assumes the gases to be a mixture of perfect
50 gases in thermal equilibrium, and assumes no reaction or condensation with the porous
51 network [1].

52 In sum, the objectives of this work are as follows:

- 53 1. Extend the previous formulation from Ref. [12] to model the transient thermo-ablative
54 response of multi-layered hypersonic TPS through a systematic coarse-graining proce-
55 dure based on the Mori-Zwanzig formalism.
- 56 2. Benchmark the accuracy, generalizability, and computational efficiency of the PIROM
57 against the RPM and the high-fidelity FEM solutions of ablating TPS, thus demon-
58 strating the PIROM's potential to solve the ITM in complex multi-physical non-linear
59 dynamical systems.

60 **2 Modeling of Ablating Thermal Protection Systems**

61 This section presents the problem of modeling a non-decomposing ablating TPS subjected to
62 extreme hypersonic heating. Two different but mathematically connected solution strategies
63 are provided: (1) a high-fidelity full-order model (FOM) based on a finite element method
64 (FEM), and (2) a low-fidelity reduced-physics model (RPM) based on a lumped capacitance
65 model (LCM) and a one-dimensional surface velocity model (SVM). The FOM is compu-
66 tationally expensive but provides the highest fidelity, while the RPM is computationally
67 efficient but has low predictive fidelity; both models are amenable to high-dimensional de-
68 sign variables. The RPM is used in the subsequent sections for deriving the PIROM.

69 **2.1 Governing Equations**

70 The multi-physics for a non-decomposing ablating TPS involves the *energy equation* which
71 models the transient heat conduction inside the TPS, and the *pseudo-elasticity equation*,

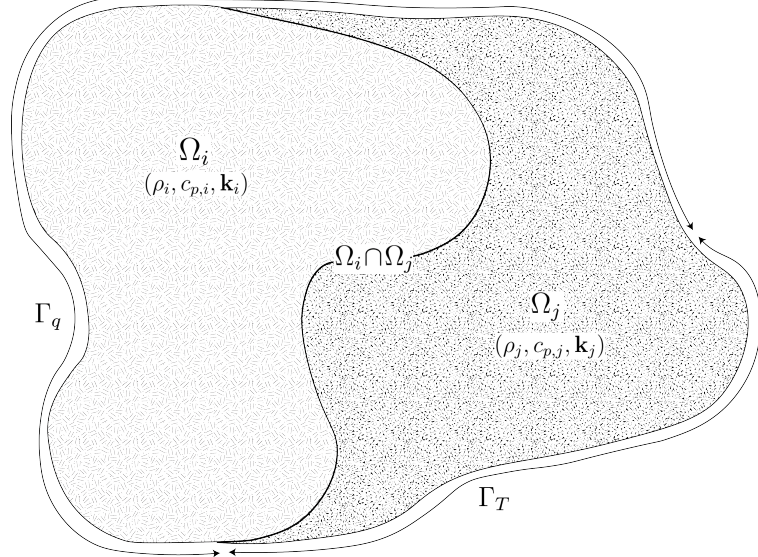


Figure 1: General domain Ω with prescribed Neumann and Dirichlet boundary conditions on Γ_q and Γ_T . Mesh displacement $w(x, t)$ occurs on the Γ_q boundary.

72 which models the mesh motion due to surface recession. The governing PDEs for the ablating
 73 TPS are summarized in this section.

74 **2.1.1 Energy Equation**

75 Consider a generic domain $\Omega \subset \mathbb{R}^d$, $d = 2$ or 3 , illustrated in Fig. 1. Let $\partial\Omega = \Gamma_q \cup \Gamma_T$ and
 76 $\Gamma_q \cap \Gamma_T = \emptyset$, where a Neumann $q_b(x, t)$ boundary condition is prescribed on the Γ_q boundary,
 77 and represents the surface exposed to the hypersonic boundary layer. The Dirichlet $T_b(x, t)$
 78 boundary condition is prescribed on the boundary Γ_T . The TPS is divided into N non-
 79 overlapping components $\{\Omega_i\}_{i=1}^N$, as illustrated in Fig. 1 for $N = 2$. The i -th component Ω_i
 80 is associated with material properties $(\rho_i, c_{p,i}, \mathbf{k}_i)$, that are assumed to be continuous within
 81 one component, and can be discontinuous across two neighboring components.

82 The transient heat conduction is described by the energy equation,

$$\rho c_p \left(\frac{\partial T}{\partial t} + \tilde{\mathbf{v}}(x, t) \cdot \nabla T \right) - \nabla \cdot (\mathbf{k} \nabla T) = 0, \quad x \in \Omega \quad (1a)$$

$$-\mathbf{k} \nabla T \cdot \mathbf{n} = q_b(x, t), \quad x \in \Gamma_q \quad (1b)$$

$$T(x, t) = T_b(x, t), \quad x \in \Gamma_T \quad (1c)$$

$$T(x, 0) = T_0(x), \quad x \in \Omega \quad (1d)$$

83 where the density ρ is constant, while the heat capacity c_p and thermal conductivity $\mathbf{k} \in \mathbb{R}^{d \times d}$
 84 may depend on temperature. In the order they appear, the terms in eq. (1a) include, the
 85 unsteady energy storage, heat conduction, temperature advection due to mesh motion, and
 86 source terms due to boundary conditions. The boundary conditions for the energy equation
 87 includes Neumann eq. (1b) and Dirichlet eq. (1c) on Γ_T .

88 An Abirtrary Lagrangian-Eulerian (ALE) description is used to account for mesh motion
 89 due to surface recession, where $\tilde{\mathbf{v}}(x, t)$ is the relative velocity of the material with respect to
 90 the mesh,

$$\tilde{\mathbf{v}}(x, t) = \mathbf{v}_s(x, t) - \mathbf{v}_m(x, t) \quad (2)$$

91 where $\mathbf{v}_s(x, t)$ and $\mathbf{v}_m(x, t)$ are the physical material velocity and mesh velocity, respectively.
 92 In this work, the physical material velocity is assumed to be zero, i.e., $\mathbf{v}_s(x, t) = \mathbf{0}$, and thus
 93 the relative velocity is simply the negative of the mesh velocity, $\tilde{\mathbf{v}}(x, t) = -\mathbf{v}_m(x, t)$.

⁹⁴ **2.1.2 Pseudo-Elasticity Equation**

⁹⁵ The mesh motion is described by the steady-state pseudo-elasticity equation without body
⁹⁶ forces,

$$\nabla \cdot \boldsymbol{\sigma}(\mathbf{w}) = \mathbf{0}, \quad \forall t \in \mathcal{T}, \mathbf{x} \in \Omega \quad (3a)$$

$$\mathbf{w}(\mathbf{x}, t) = \mathbf{w}_q(\mathbf{x}, t), \quad \forall t \in \mathcal{T}, \mathbf{x} \in \Gamma_q \quad (3b)$$

$$\mathbf{w}(\mathbf{x}, t) = \mathbf{0}, \quad \forall t \in \mathcal{T}, \mathbf{x} \notin \Gamma_q \quad (3c)$$

$$\mathbf{w}(\mathbf{x}, 0) = \mathbf{0}, \quad \forall \mathbf{x} \in \Omega \quad (3d)$$

⁹⁷ where the stress tensor $\boldsymbol{\sigma}$ is related to the strain tensor $\boldsymbol{\epsilon}(\mathbf{w})$ through Hooke's law,

$$\boldsymbol{\sigma}(\mathbf{w}) = \mathbb{D} : \boldsymbol{\epsilon}(\mathbf{w})$$

⁹⁸ where \mathbb{D} is the fourth-order positive definite elasticity tensor, and ":" is the double con-
⁹⁹ traction of the full-order tensor \mathbb{D} with the second-order tensor $\boldsymbol{\epsilon}$. The elasticity tensor
¹⁰⁰ ordinarily possess a number of symmetries, effectively reducing the number of components
¹⁰¹ that describe it [2]. The symmetric strain tensor $\boldsymbol{\epsilon}$ measures the deformation of the mesh
¹⁰² due to displacements $\mathbf{w}(x, t)$, and is defined as,

$$\boldsymbol{\epsilon}(\mathbf{w}) = \frac{1}{2} (\nabla \mathbf{w} + \nabla \mathbf{w}^\top)$$

¹⁰³ The "material" properties for the mesh are chosen to tailor the mesh deformation, and need
¹⁰⁴ not represent the actual material being modeled [1].

¹⁰⁵ For the pseudo-elasticity equations, the boundary conditions include prescribed displace-
¹⁰⁶ ments $\mathbf{w}_q(x, t)$ on the heated boundary Γ_q in eq. (3b), and zero displacements on the unheated
¹⁰⁷ boundaries in eq. (3c). The initial condition for the mesh displacements is zero in eq. (3d).
¹⁰⁸ Particularly, the surface velocity due to the ablating material is a function of the surface

¹⁰⁹ temperature $T_q(x, t)$ for $x \in \Gamma_q$ on the heated boundary. For the i -th material component,
¹¹⁰ the mesh velocity on the heated boundary is imposed based on the following relation,

$$\hat{\mathbf{n}} \cdot \mathbf{v}_m(x, t) = f(T_q(x, t)), \quad x \in \Gamma_q \quad (4)$$

¹¹¹ where $\hat{\mathbf{n}}$ is the unit normal vector on the heated boundary Γ_q , and f is a function obtained
¹¹² from tabulated data for the material, commonly referred to as a B' table [1]. The B' table
¹¹³ provides a model for the recession velocity as a function of the surface temperature, and is
¹¹⁴ pre-computed based on high-fidelity simulations of the ablation process for a one-dimensional
¹¹⁵ slab of the material, and is independent of the TPS geometry. Provided the surface velocity,
¹¹⁶ the boundary condition in eq. (5) for the mesh displacements are computed by integrating
¹¹⁷ the surface velocity over time,

$$\mathbf{w}_q(x, t) = \int_0^t \mathbf{v}_m(x, \tau) d\tau \quad (5)$$

¹¹⁸ 2.2 Full-Order Model: Finite-Element Method

¹¹⁹ To obtain the full-order numerical solution, the *energy equation* is spatially discretized using
¹²⁰ variational principles of the Discontinuous Galerkin (DG) method [5]. Note that the choice
¹²¹ of DG approach is mainly for theoretical convenience, and is exclusively performed on the
¹²² energy equation, as it is the surface temperature that drives the ablation process. The
¹²³ equivalence between DG and FEM is noted upon their convergence. For the *pseudo-elasticity*
¹²⁴ *equation* standard FEM is used to compute the mesh displacements based on the surface
¹²⁵ temperature provided by the DG solution of the energy equation [2].

¹²⁶ Consider a conforming mesh partition domain, where each element belongs to one and
¹²⁷ only one component. Denote the collection of all M elements as $\{E_i\}_{i=1}^M$. In an element E_i ,
¹²⁸ its shared boundaries with another element E_j , Neumann BC, and Dirichlet BC are denoted
¹²⁹ as e_{ij} , e_{iq} , and e_{iT} , respectively. Lastly, $|e|$ denotes the length ($n_d = 2$) or area ($n_d = 3$) of a

¹³⁰ component boundary e .

¹³¹ For the i -th element, use a set of P trial functions, such as polynomials, to represent the
¹³² temperature distribution,

$$T_i(x, t) = \sum_{l=1}^P \phi_l^i(x) u_l^i(t) \equiv \boldsymbol{\phi}_i^\top(x) \mathbf{u}_i(t), \quad i = 1, 2, \dots, M \quad (6)$$

¹³³ Without loss of generality, the trial functions are assumed to be orthogonal, so that,

$$\int_{E_i} \phi_l^i(x) \phi_k^i(x) d\Omega = 0, \quad l \neq k$$

¹³⁴ where δ_{lk} is the Kronecker delta function. Furthermore, for simplicity, choose $\phi_1^i = 1$. Thus,
¹³⁵ by orthogonality,

$$\int_{E_i} \phi_1^i(x) d\Omega = |E_i|, \quad \int_{E_i} \phi_k^i(x) d\Omega = 0, \quad k = 2, 3, \dots, P$$

¹³⁶ Under the choice of basis functions, u_1^i is simply the average temperature of element E_i ,
¹³⁷ denoted as \bar{u}_i .

¹³⁸ By standard variational processes, e.g., [5], the element-wise governing equation is de-
¹³⁹ noted as,

$$\mathbf{A}_i \dot{\mathbf{u}}_i = (\mathbf{B}_i + \mathbf{C}_i) \mathbf{u}_i + \sum_{j \in \mathcal{N}_i \cup \{T_b\}} (\mathbf{B}_{ij}^i \mathbf{u}_i + \mathbf{B}_{ij}^j \mathbf{u}_j) + \mathbf{f}_i(t), \quad \text{for } i = 1, 2, \dots, M \quad (7)$$

¹⁴⁰ which is collected as the following ODE for all the elements in the mesh,

$$\mathbf{A}(\mathbf{u}) \dot{\mathbf{u}} = [\mathbf{B}(\mathbf{u}) + \mathbf{C}(\mathbf{u})] \mathbf{u} + \mathbf{f}(t) \quad (8)$$

¹⁴¹ where $\mathbf{u} = [\mathbf{u}_1, \mathbf{u}_2, \dots, \mathbf{u}_M]^\top \in \mathbb{R}^{MP}$ includes all the DG variables, $\mathbf{f} \in \mathbb{R}^{MP}$ is the exter-
¹⁴² nal forcing, and the system matrices \mathbf{A} , \mathbf{B} , and \mathbf{C} are the matrices due to heat capacity,
¹⁴³ heat conduction, and temperature advection due to mesh motion, respectively. A detailed

¹⁴⁴ derivation of eqs. (7) and (8) and their matrices is provided in Appendix A.

¹⁴⁵ 2.3 Reduced-Physics Model

¹⁴⁶ The RPM for predicting the response of the ablating TPS consists of two components: (1)
¹⁴⁷ the *lumped-capacitance model* (LCM), and (2) the *surface velocity model* (SVM). The LCM is
¹⁴⁸ described as a first-order system of ODEs for predicting the average temperatures inside the
¹⁴⁹ components of the TPS, and provides a low-fidelity (under estimate) for the component's
¹⁵⁰ surface temperature. The SVM provides a relation between the surface temperature and
¹⁵¹ the surface recession velocity based on pre-computed B' tables for the material, enabling the
¹⁵² computation of one-dimensional surface displacements. The LCM and SVM are combined to
¹⁵³ define the RPM, providing low-fidelity estimates for the temperatures and surface recession
¹⁵⁴ of the ablating TPS.

¹⁵⁵ 2.3.1 Lumped Capacitance Model

¹⁵⁶ A general form of the LCM is provided in this section; details regarding the derivation for
¹⁵⁷ the four-component TPS in Fig. ?? are provided in Appendix A. The LCM is a classical
¹⁵⁸ physics-based low-order model for predicting the temporal variation of average temperature
¹⁵⁹ in multiple interconnected components [7]. The LCM is derived at the component level from
¹⁶⁰ a point of view of energy conservation, and leads to the following system of ODEs for the
¹⁶¹ average temperatures on the components,

$$\bar{\mathbf{A}}\dot{\bar{\mathbf{u}}} = \bar{\mathbf{B}}\bar{\mathbf{u}} + \bar{\mathbf{f}}(t) \quad (9)$$

¹⁶² Where the states and inputs,

$$\bar{\mathbf{u}} = [\bar{u}_1, \bar{u}_2, \dots, \bar{u}_N]^\top \in \mathbb{R}^N, \quad \bar{\mathbf{f}} = [\bar{f}_1, \bar{f}_2, \dots, \bar{f}_N]^\top \in \mathbb{R}^N \quad (10)$$

¹⁶³ include the average temperatures $\bar{\mathbf{u}}$ and spatially-integrated inputs $\bar{\mathbf{f}}$ for the N components.
¹⁶⁴ For $i, j = 1, 2, \dots, N$ the (i, j) -th elements of the $\bar{\mathbf{A}} \in \mathbb{R}^{N \times N}$, $\bar{\mathbf{B}} \in \mathbb{R}^{N \times N}$, and $\bar{\mathbf{f}} \in \mathbb{R}^N$
¹⁶⁵ matrices are given by,

$$\bar{A}_i = \begin{cases} \int_{\Omega_i} \rho c_p d\Omega_i, & i = j \\ 0, & i \neq j \end{cases}, \quad \bar{B}_{ij} = \begin{cases} \sum_{j \in \mathcal{N}_i \cup \{T_b\}} \bar{B}_{ij}^i, & i = j \\ \bar{B}_{ij}^{(j)}, & i \neq j \end{cases}, \quad (11a)$$

$$\mathbf{f}_i = \begin{cases} |e_{iq}| \bar{q}_i + \frac{|e_{iT}|}{R_i} \bar{T}_i, & i = j \\ 0, & i \neq j \end{cases} \quad (11b)$$

¹⁶⁶ where,

$$\bar{q}_i = \frac{1}{|e_{iq}|} \int_{e_{iq}} q_b de_{iq}, \quad \bar{T}_i = \frac{1}{|e_{iT}|} \int_{e_{iT}} T_b de_{iT}, \quad \bar{B}_{ij}^i = -\frac{|e_{ij}|}{R_{ij}}, \quad \bar{B}_{ij}^j = \frac{|e_{ij}|}{R_{ij}} \quad (12)$$

¹⁶⁷ where R_{ij} is the equivalent thermal resistance between two neighboring components Ω_i and
¹⁶⁸ Ω_j , and R_i is the thermal resistance between component Ω_i and the Dirichlet boundary.
¹⁶⁹ The thermal resistances are computed based on the geometry and material properties of the
¹⁷⁰ components; details regarding their computation are provided in Appendix A.

¹⁷¹ 2.3.2 Surface Velocity Model

¹⁷² The displacement is assumed to be *one-dimensional* on the heated boundary Γ_q , i.e., the
¹⁷³ surface recedes only in the direction of the applied load. For example, in Fig. ??, the surface
¹⁷⁴ displacement on the heated boundary occurs only in the negative y -direction for the three
¹⁷⁵ components exposed to the hypersonic boundary layer; the fourth component is the substrate
¹⁷⁶ and does not ablate. Displacements along the x direction is small relative to displacements
¹⁷⁷ in the y direction, and are thus neglected.

¹⁷⁸ For the i -th ablating component, the SVM considered in this work takes the form,

$$\dot{\mathbf{w}} = \Xi \bar{\mathbf{u}} - \tilde{\mathbf{f}} \quad (13)$$

¹⁷⁹ where $\Xi = \text{diag}(\alpha_1, \dots, \alpha_{\tilde{N}})$ and $\tilde{\mathbf{f}} = (\alpha_1 \bar{u}_{0,1}, \dots, \alpha_{\tilde{N}} \bar{u}_{0,\tilde{N}})^\top$. The constants α_i are small
¹⁸⁰ material-dependent constants, determined from the B' table, and $\bar{u}_{0,i}$ is the constant initial
¹⁸¹ temperature of the ablative component. The SVM provides a relation between the surface's
¹⁸² temperature and recession velocity, based on pre-computed B' tables for the material.

¹⁸³ **2.3.3 Coupled Reduced-Physics Model**

¹⁸⁴ The LCM and SVM are combined to define the RPM for predicting the thermo-ablative
¹⁸⁵ response of the TPS under hypersonic boundary layers. Specifically, the RPM is defined as
¹⁸⁶ the LCM as in eq. (9), where the *geometry- and temperature-dependent matrices* $\bar{\mathbf{A}}$, $\bar{\mathbf{B}}$, and
¹⁸⁷ $\bar{\mathbf{f}}$ are updated at each time step based on the current temperature $\bar{\mathbf{u}}$ and displacements \mathbf{w}
¹⁸⁸ provided by the SVM. The RPM is formally stated as,

$$\tilde{\mathbf{A}}(\mathbf{s})\dot{\mathbf{s}} = \tilde{\mathbf{B}}(\mathbf{s})\mathbf{s} + \tilde{\mathbf{F}}(t) \quad (14a)$$

$$\tilde{\mathbf{z}} = \mathbf{I}\mathbf{s} \quad (14b)$$

¹⁸⁹ where the state $\mathbf{s} = [\bar{\mathbf{u}}, \mathbf{w}]^\top \in \mathbb{R}^{2N}$ includes the *average temperature* and *one-dimensional*
¹⁹⁰ *surface displacements*; these are used in the observable outputs $\mathbf{z} = [\bar{\mathbf{u}}, \mathbf{w}]^\top \in \mathbb{R}^{N+\tilde{N}}$, where
¹⁹¹ \tilde{N} is the number of ablating components and $\tilde{N} \leq N$. The matrices are given as,

$$\tilde{\mathbf{A}}(\mathbf{s}) = \begin{bmatrix} \bar{\mathbf{A}}(\mathbf{s}) & \mathbf{0} \\ \mathbf{0} & \mathbf{I} \end{bmatrix}, \quad \tilde{\mathbf{B}}(\mathbf{s}) = \begin{bmatrix} \bar{\mathbf{B}}(\mathbf{s}) & \mathbf{0} \\ \Xi & \mathbf{0} \end{bmatrix}, \quad \tilde{\mathbf{F}}(t) = \begin{bmatrix} \bar{\mathbf{f}}(t) \\ -\tilde{\mathbf{f}} \end{bmatrix} \quad (15)$$

¹⁹² In the matrices $\tilde{\mathbf{A}}$ and $\tilde{\mathbf{B}}$, the surface displacements \mathbf{w} are used to define the dimensions for
¹⁹³ the Ω_i component used in eqs. (11b) and (12), thus effectively coupling the LCM and SVM.

¹⁹⁴ **2.4 Summary of Modeling Approaches**

¹⁹⁵ The FOM (i.e., FEM) and RPM (i.e., LCM with SVM) are two different but mathemati-
¹⁹⁶ cally connected solution strategies. Particularly, the LCM in eq. (9) not only resembles the
¹⁹⁷ functional form of the DG model in eq. (8), but can be viewed as a special case of the latter,
¹⁹⁸ where the mesh partition is extremely coarse, and the trial and test functions are piece-wise
¹⁹⁹ constants. This removes all spatial variations within each component, and neglects advection
²⁰⁰ effects due to mesh motion.

²⁰¹ For example, consider the case where each component Ω_i is treated as one single element,
²⁰² and each element employs one constant basis function $\phi_i = 1$. The element-wise DG model
²⁰³ in eq. (7) simplifies into a scalar ODE,

$$\mathbf{A}^{(i)} = \bar{A}_i, \quad \mathbf{C}^{(i)} = 0, \quad \mathbf{B}_{ij}^{(i)} = -\sigma|e_{ij}|, \quad \mathbf{B}_{ij}^{(j)} = \sigma|e_{ij}|, \quad \mathbf{f}_i = |e_{iq}|\bar{q}_i + \sigma|e_{iT}|\bar{T}_i \quad (16)$$

²⁰⁴ Clearly, the LCM is a coarse zeroth-order DG model with the inverse of thermal resistance
²⁰⁵ chosen as the element-wise penalty factors. Or conversely, the DG model is a refined version
²⁰⁶ of LCM via *hp*-adaptation.

²⁰⁷ The FOM and RPM represent two extremes in the modeling fidelity and computational
²⁰⁸ cost spectrum. On one hand, the FOM is the most accurate but computationally expensive
²⁰⁹ to evaluate due to the fine mesh discretizations for both the temperature and displacement
²¹⁰ fields, leading to possibly millions of state variables. On the other hand, the RPM consid-
²¹¹ ers only the average temperature of the material, from which the one-dimensional surface
²¹² displacements are computed by integrating eq. (13). This considerably reduces the com-
²¹³ putational cost, but sacrifices local temperature information that are critical to properly
²¹⁴ capture higher-order effects due to mesh motion and thermal gradients within each compo-
²¹⁵ nent. Thus, neither the FOM nor the RPM is an universal approach for real-world analysis,
²¹⁶ design, and optimization tasks for ablating TPS, where thousands of high-fidelity model
²¹⁷ evaluations may be necessary. This issue motivates the development of the PIROM, which

218 can achieve the fidelity of FOM at a computational cost close to the RPM, while maintaining
219 the generalizability to model parameters.

220 3 Physics-Infused Reduced-Order Modeling

221 The formulation of PIROM for ablating TPS starts by connecting the FOM, i.e., the DG-
222 FEM, and the RPM, i.e., the LCM, via a coarse-graining procedure. This procedure pin-
223 points the missing dynamics in the LCM when compared to DG-FEM. Subsequently, the
224 Mori-Zwanzig (MZ) formalism is employed to determine the model form for the missing dy-
225 namics in PIROM. Lastly, the data-driven identification of the missing dynamics in PIROM
226 is presented.

227 3.1 Deriving the Reduced-Physics Model via Coarse-Graining

228 The subsequent coarse-graining formulation is performed on the DG-FEM in eq. (8) to derive
229 the LCM in eq. (9). This process constraints the trial function space of a full-order DG model
230 to a subset of piece-wise constants, so that the variables \mathbf{u} , matrices \mathbf{A} , \mathbf{B} , and \mathbf{C} , and forcing
231 vector \mathbf{f} are all approximated using a single state associated to the average temperature.
232 Note that the coarse-graining is exclusively performed on the thermal dynamics, as it is
233 the surface temperature that drives the one-dimensional recession via the SVM. Hence, the
234 coarse-graining of the mesh dynamics is not included in the following procedure.

235 3.1.1 Coarse-Graining of States

236 Consider a DG model as in eq. (8) for M elements and an LCM as in eq. (9) for N components;
237 clearly $M \gg N$. Let $\mathcal{V}_j = \{i | E_i \in \Omega_j\}$ be the indices of the elements belonging to the j -th
238 component, so $E_i \in \Omega_j$ for all $i \in \mathcal{V}_j$. The number of elements in the j -th component is $|\mathcal{V}_j|$.

²³⁹ The average temperature on Ω_j is,

$$\bar{u}_j = \frac{1}{|\Omega_j|} \sum_{i \in \mathcal{V}_j} \int_{E^{(i)}} \boldsymbol{\phi}^{(i)}(x)^T \mathbf{u}^{(i)} d\Omega = \frac{1}{|\Omega_j|} \sum_{i \in \mathcal{V}_j} |E_i| \boldsymbol{\varphi}_i^{j\top} \mathbf{u}^{(i)}, \quad j = 1, 2, \dots, N \quad (17)$$

²⁴⁰ where $|\Omega_j|$ and $|E_i|$ denote the area ($d = 2$) or volume ($d = 3$) of component j and element ²⁴¹ i , respectively. The orthogonal basis functions are defined as $\boldsymbol{\varphi}_i^{j\top} = [1, 0, \dots, 0]^\top \in \mathbb{R}^P$.

²⁴² Conversely, given the average temperatures of the N components, $\bar{\mathbf{u}}$, the states of an ²⁴³ arbitrary element E_i is written as,

$$\mathbf{u}^{(i)} = \sum_{k=1}^N \boldsymbol{\varphi}_i^k \bar{u}_k + \delta \mathbf{u}^{(i)}, \quad i = 1, 2, \dots, M \quad (18)$$

²⁴⁴ where $\boldsymbol{\varphi}_i^k = 0$ if $i \notin \mathcal{V}_k$, and $\delta \mathbf{u}^{(i)}$ represents the deviation from the average temperature and ²⁴⁵ satisfies the orthogonality condition $\boldsymbol{\varphi}_i^k \delta \mathbf{u}^{(i)} = 0$ for all k .

²⁴⁶ Equations eqs. (17) and (18) are combined and written in matrix form as,

$$\bar{\mathbf{u}} = \boldsymbol{\Phi}^+ \mathbf{u}, \quad \mathbf{u} = \boldsymbol{\Phi} \mathbf{u} + \delta \mathbf{u} \quad (19)$$

²⁴⁷ where $\boldsymbol{\Phi} \in \mathbb{R}^{MP \times N}$ is a matrix of $M \times N$ blocks, with the (i, j) -th block as $\boldsymbol{\varphi}_i^j$, $\boldsymbol{\Phi}^+ \in \mathbb{R}^{N \times MP}$ ²⁴⁸ is the left inverse of $\boldsymbol{\Phi}$, with the (i, j) -th block as $\boldsymbol{\varphi}_i^{j+} = \frac{|E_i|}{|\Omega_j|} \boldsymbol{\varphi}_i^{j\top}$, and $\delta \mathbf{u}$ is the collection of ²⁴⁹ deviations. By their definitions, $\boldsymbol{\Phi}^+ \boldsymbol{\Phi} = \mathbf{I}$ and $\boldsymbol{\Phi}^+ \delta \mathbf{u} = \mathbf{0}$.

²⁵⁰ 3.1.2 Coarse-Graining of Dynamics

²⁵¹ The dependence of the matrices with respect to the displacements \mathbf{w} is dropped to isolate ²⁵² the analysis based on coarsened variables. Consider a function of states in the form of ²⁵³ $\mathbf{M}(\mathbf{u}) \mathbf{g}(\mathbf{u})$, where $\mathbf{g} : \mathbb{R}^{MP} \rightarrow \mathbb{R}^{MP}$ is a vector-valued function, and $\mathbf{M} : \mathbb{R}^{MP} \rightarrow \mathbb{R}^{p \times MP}$ ²⁵⁴ is a matrix-valued function with an arbitrary dimension p . Define the projection matrix

255 $\mathbf{P} = \Phi\Phi^+$ and the projection operator \mathcal{P} as,

$$\begin{aligned}\mathcal{P}[\mathbf{M}(\mathbf{u})\mathbf{g}(\mathbf{u})] &= \mathbf{M}(\mathbf{P}\mathbf{u})\mathbf{g}(\mathbf{P}\mathbf{u}) \\ &= \mathbf{M}(\Phi\bar{\mathbf{u}})\mathbf{g}(\Phi\bar{\mathbf{u}})\end{aligned}\quad (20)$$

256 so that the resulting function depends only on the average temperatures $\bar{\mathbf{u}}$. Correspondingly,
257 the residual operator $\mathcal{Q} = \mathcal{I} - \mathcal{P}$, and $\mathcal{Q}[\mathbf{M}(\mathbf{u})\mathbf{g}(\mathbf{u})] = \mathbf{M}(\mathbf{u})\mathbf{g}(\mathbf{u}) - \mathbf{M}(\Phi\bar{\mathbf{u}})\mathbf{g}(\Phi\bar{\mathbf{u}})$. When
258 the function is not separable, the projection operator is simply defined as $\mathcal{P}[\mathbf{g}(\mathbf{u})] = \mathbf{g}(\mathbf{P}\mathbf{u})$.

259 Subsequently, the operators defined above are applied to coarse-grain the dynamics. First,
260 write the DG-FEM in eq. (8) as,

$$\dot{\mathbf{u}} = \mathbf{A}(\mathbf{u})^{-1}\mathbf{B}(\mathbf{u})\mathbf{u} + \mathbf{A}(\mathbf{u})^{-1}\mathbf{C}(\mathbf{u})\mathbf{u} + \mathbf{A}(\mathbf{u})^{-1}\mathbf{f}(t) \quad (21)$$

261 and multiply both sides by Φ^+ to obtain,

$$\Phi^+\dot{\mathbf{u}} = \Phi^+(\Phi\dot{\bar{\mathbf{u}}} + \delta\dot{\mathbf{u}}) = \dot{\bar{\mathbf{u}}} = \Phi^+\mathbf{r}(\mathbf{u}, t) \quad (22)$$

262 Apply the projection operator \mathcal{P} and the residual operator \mathcal{Q} to the right-hand side to obtain,

$$\dot{\bar{\mathbf{u}}} = \mathcal{P}[\Phi^+\mathbf{r}(\mathbf{u}, t)] + \mathcal{Q}[\Phi^+\mathbf{r}(\mathbf{u}, t)] \equiv \mathbf{r}^{(1)}(\mathbf{u}, t) + \mathbf{r}^{(2)}(\mathbf{u}, t) \quad (23)$$

263 where $\mathbf{r}^{(1)}(\mathbf{u}, t)$ is resolved dynamics that depends on $\bar{\mathbf{u}}$ only, and $\mathbf{r}^{(2)}(\mathbf{u}, t)$ is the un-resolved
264 or residual dynamics. Detailed derivations and analysis of $\mathbf{r}^{(1)}(\mathbf{u}, t)$ and $\mathbf{r}^{(2)}(\mathbf{u}, t)$ can be
265 found in the Appendix.

266 It follows from Ref. [12] that the resolved dynamics is exactly the LCM, where the
267 advection term reduces to zero, i.e., $\bar{\mathbf{C}}(\bar{\mathbf{u}}) = \mathbf{0}$ as shown in the Appendix. Using the notation

268 from eq. (9), it follows that,

$$\begin{aligned}\mathbf{r}^{(1)}(\mathbf{u}, t) &= \bar{\mathbf{A}}(\bar{\mathbf{u}})^{-1}\bar{\mathbf{B}}(\bar{\mathbf{u}})\bar{\mathbf{u}} + \bar{\mathbf{A}}(\bar{\mathbf{u}})^{-1}\bar{\mathbf{C}}(\bar{\mathbf{u}})\bar{\mathbf{u}} + \bar{\mathbf{A}}(\bar{\mathbf{u}})^{-1}\bar{\mathbf{f}}(\bar{\mathbf{u}}) \\ &= \bar{\mathbf{A}}(\bar{\mathbf{u}})^{-1}\bar{\mathbf{B}}(\bar{\mathbf{u}})\bar{\mathbf{u}} + \bar{\mathbf{A}}(\bar{\mathbf{u}})^{-1}\bar{\mathbf{f}}(t)\end{aligned}\quad (24)$$

269 where the following relations hold,

$$\bar{\mathbf{A}}(\bar{\mathbf{u}}) = \mathbf{W} (\Phi^+ \mathbf{A} (\Phi \bar{\mathbf{u}})^{-1} \Phi)^{-1} \quad \bar{\mathbf{C}}(\bar{\mathbf{u}}) = \mathbf{0} \quad (25a)$$

$$\bar{\mathbf{B}}(\bar{\mathbf{u}}) = \mathbf{W} \Phi^+ \mathbf{B} (\Phi \bar{\mathbf{u}}) \Phi \quad \bar{\mathbf{f}}(t) = \mathbf{W} \Phi^+ \mathbf{f} \quad (25b)$$

270 where $\mathbf{W} \in \mathbb{R}^{N \times N}$ is a diagonal matrix with the i -th element as $[\mathbf{W}]_{ii} = |\mathcal{V}_k|$ if $i \in \mathcal{V}_k$.

271 The examination of the second residual term $\mathbf{r}^{(2)}(\mathbf{u}, t)$ in eq. (23) is shown in the Appendix,
272 and demonstrates that the physical sources of missing dynamics in the LCM include: the
273 approximation of non-uniform temperature within each component as a constant, and the
274 elimination of the advection term due to coarse-graining. In sum, the above results not
275 only show that the LCM is a result of coarse-graining of the full-order DG-FEM, but also
276 reveal the discrepancies between the LCM and the DG-FEM. These discrepancies propagate
277 into the SVM, which as a result of the averaging in the LCM formulation, under-predicts
278 the surface recession rates. In the subsequent section, the discrepancies in the LCM are
279 corrected to formulate the PIROM.

280 3.2 Physics-Infusion Via Mori-Zwanzig Formalism

281 The Mori-Zwanzig (MZ) formalism is an operator-projection technique used to derive ROMs
282 for high-dimensional dynamical systems, especially in statistical mechanics and fluid dynam-
283 ics [9, 10, 11]. It provides an exact reformulation of a high-dimensional Markovian dynamical
284 system, into a low-dimensional observable non-Markovian dynamical system. The proposed
285 ROM is subsequently developed based on the approximation to the non-Markovian term in

the observable dynamics. Particularly, eq. (23) shows that the DG-FEM dynamics can be decomposed into the resolved dynamics $\mathbf{r}^{(1)}(\mathbf{u}, t)$ and the orthogonal dynamics $\mathbf{r}^{(2)}(\mathbf{u}, t)$, in the sense of $\mathcal{P}\mathbf{r}^{(2)} = 0$. In this case, the MZ formalism can be invoked to express the dynamics $\bar{\mathbf{u}}$ in terms of $\bar{\mathbf{u}}$ alone as the projected Generalized Langevin Equation (GLE) [9, 10, 11],

$$\dot{\bar{\mathbf{u}}}(t) = \mathbf{r}^{(1)}(\bar{\mathbf{u}}, t) + \int_0^t \tilde{\kappa}(t, s, \bar{\mathbf{u}}) ds \quad (26)$$

where the first and second terms are referred to as the Markovian and non-Markovian terms, respectively. The non-Markovian term accounts for the effects of past un-resolved states on the current resolved states via a memory kernel $\tilde{\kappa}(t, s, \bar{\mathbf{u}})$, which in practice is computationally expensive to evaluate.

3.2.1 Markovian Reformulation

This section details the formal derivation of the PIROM as a system of ODEs for the thermal dynamics, based on approximations to the memory kernel. Specifically, the kernel $\tilde{\kappa}$ is examined via a leading-order expansion, based on prior work [13]; this can be viewed as an analog of zeroth-order holding in linear system theory with a sufficiently small time step. In this case, the memory kernel is approximated as,

$$\tilde{\kappa}(t, s, \bar{\mathbf{u}}) \approx \mathbf{r}^{(1)}(\bar{\mathbf{u}}, t) \cdot \nabla_{\bar{\mathbf{u}}} \mathbf{r}^{(2)}(\Phi \bar{\mathbf{u}}, t) \quad (27)$$

Note that the terms in $\mathbf{r}^{(1)}$ have a common factor $\bar{\mathbf{A}}^{-1}$; this motivates the following heuristic modification of the model form in eq. (26),

$$\dot{\bar{\mathbf{u}}} = \mathbf{r}^{(1)}(\bar{\mathbf{u}}, t) + \bar{\mathbf{A}}^{-1}(\bar{\mathbf{u}}) \int_0^t \kappa(t, s, \bar{\mathbf{u}}) ds \quad (28a)$$

$$\bar{\mathbf{A}}(\bar{\mathbf{u}}) \dot{\bar{\mathbf{u}}} = \bar{\mathbf{B}}(\bar{\mathbf{u}}) \bar{\mathbf{u}} + \bar{\mathbf{f}}(t) + \int_0^t \kappa(t, s, \bar{\mathbf{u}}) ds \quad (28b)$$

302 where the original kernel $\tilde{\kappa}$ is effectively normalized by $\bar{\mathbf{A}}^{-1}$. Intuitively, such choice of kernel
 303 reduces its dependency on the averaged material properties, and simplifies the subsequent
 304 design of model form.

305 Subsequently, the hidden states are introduced to “Markovianize” the system eq. (26).
 306 In this manner, eq. (28b) is converted into a pure state-space model, with the functional
 307 form of the LCM retained; since LCM is a physics-based model, then it encodes the phys-
 308 ical information and retains explicit parametric dependence of the problem. Consider the
 309 representation of the kernel as a finite sum of simpler functions, e.g., exponentials,

$$\kappa(t, s, \bar{\mathbf{u}}) = \sum_{j=1}^m \mathcal{K}_j(t, s, \bar{\mathbf{u}}) [\mathbf{p}_j + \mathbf{d}_j(\bar{\mathbf{u}})] \phi_j(s, \bar{\mathbf{u}}) \quad (29)$$

310 where,

$$\mathcal{K}_j(t, s, \bar{\mathbf{u}}) = e^{-\int_s^t (\lambda_j + e_j(\bar{\mathbf{u}})) d\tau}, \quad \phi_j(s, \bar{\mathbf{u}}) = \mathbf{q}_j^\top \bar{\mathbf{u}}(s) + \mathbf{g}_j(\bar{\mathbf{u}})^\top \bar{\mathbf{u}}(s) + \mathbf{r}_j^\top \bar{\mathbf{f}}(s) \quad (30)$$

311 with suitable coefficients $\mathbf{p}_j, \mathbf{d}_j, \mathbf{q}_j, \mathbf{g}_j, \mathbf{r}_j \in \mathbb{R}^N$ and decay rates $\lambda_j, e_j(\bar{\mathbf{u}}) > 0$, that need to
 312 be identified from data.

313 Define the hidden states as,

$$\beta_j(t) = \int_0^t \mathcal{K}_j(s, \bar{\mathbf{u}}) \phi_j(s, \bar{\mathbf{u}}) ds \quad (31)$$

314 and differentiate with respect to time,,

$$\dot{\beta}_j(t) = -[\lambda_j + e_j(\bar{\mathbf{u}})] \beta_j(t) + \mathbf{q}_j^\top \bar{\mathbf{u}}(t) + \mathbf{g}_j(\bar{\mathbf{u}})^\top \bar{\mathbf{u}}(t) + \mathbf{r}_j^\top \bar{\mathbf{f}}(t) \quad (32)$$

315 to obtain the memory,

$$\int_0^t \kappa(t, s, \bar{\mathbf{u}}) ds = \sum_{j=1}^m [\mathbf{p}_j + \mathbf{d}_j(\bar{\mathbf{u}})] \beta_j(t) \quad (33)$$

³¹⁶ Then, eq. (28b) is recast as the extended Markovian system,

$$\bar{\mathbf{A}}(\bar{\mathbf{u}})\dot{\bar{\mathbf{u}}} = \bar{\mathbf{B}}(\bar{\mathbf{u}})\bar{\mathbf{u}} + [\mathbf{P} + \mathbf{D}(\bar{\mathbf{u}})]\boldsymbol{\beta} + \bar{\mathbf{f}}(t) \quad (34a)$$

$$\dot{\boldsymbol{\beta}} = [\mathbf{Q} + \mathbf{G}(\bar{\mathbf{u}})]\bar{\mathbf{u}} + [\mathbf{E}(\bar{\mathbf{u}}) - \boldsymbol{\Lambda}]\boldsymbol{\beta} + \mathbf{R}\bar{\mathbf{f}}(t) \quad (34b)$$

³¹⁷ where the data-driven operators associated to the hidden dynamics are collected as,

$$\boldsymbol{\Lambda} = \text{diag}(\lambda_1, \lambda_2, \dots, \lambda_m) \in \mathbb{R}^{m \times m}, \quad \mathbf{P} = [\mathbf{p}_1, \mathbf{p}_2, \dots, \mathbf{p}_m] \in \mathbb{R}^{N \times m} \quad (35a)$$

$$\mathbf{D}(\bar{\mathbf{u}}) = [\mathbf{d}_1(\bar{\mathbf{u}}), \mathbf{d}_2(\bar{\mathbf{u}}), \dots, \mathbf{d}_m(\bar{\mathbf{u}})] \in \mathbb{R}^{N \times m}, \quad \mathbf{Q} = [\mathbf{q}_1, \mathbf{q}_2, \dots, \mathbf{q}_m] \in \mathbb{R}^{m \times N} \quad (35b)$$

$$\mathbf{G}(\bar{\mathbf{u}}) = [\mathbf{g}_1(\bar{\mathbf{u}}), \mathbf{g}_2(\bar{\mathbf{u}}), \dots, \mathbf{g}_m(\bar{\mathbf{u}})] \in \mathbb{R}^{m \times N}, \quad \mathbf{R} = [\mathbf{r}_1, \mathbf{r}_2, \dots, \mathbf{r}_m] \in \mathbb{R}^{m \times N} \quad (35c)$$

$$\mathbf{E}(\bar{\mathbf{u}}) = \text{diag}(e_1(\bar{\mathbf{u}}), e_2(\bar{\mathbf{u}}), \dots, e_m(\bar{\mathbf{u}})) \in \mathbb{R}^{m \times m} \quad (35d)$$

³¹⁸ The form of the temperature-dependent matrices $\mathbf{D}(\bar{\mathbf{u}})$, $\mathbf{G}(\bar{\mathbf{u}})$, and $\mathbf{E}(\bar{\mathbf{u}})$ is specified in the
³¹⁹ next section. Since the hidden states $\boldsymbol{\beta}$ serve as the memory, their initial conditions are set
³²⁰ to zero, i.e., $\boldsymbol{\beta}(t_0) = \mathbf{0}$, no memory at the beginning. The physics-infused model in eq. (34b)
³²¹ retains the structure of the LCM, while the hidden states account for missing physics through
³²² corrections to the stiffness and advection matrices, as well as the forcing term.

³²³ 3.2.2 Coupled Physics-Infused Model

³²⁴ The next step involves coupling the physics-infused model in eq. (34b) with the SVM in
³²⁵ eq. (13) to define the PIROM for ablating TPS. To this end, define the observables as the
³²⁶ surface temperature $\mathbf{z}_u \in \mathbb{R}^{\tilde{N}}$ and displacements $\mathbf{z}_w \in \mathbb{R}^{\tilde{N}}$ for $\tilde{N} \leq N$ ablating components
³²⁷ to define the observable vector as $\mathbf{z} = [\mathbf{z}_u, \mathbf{z}_w]^\top \in \mathbb{R}^{n_z}$ with $n_z = 2\tilde{N}$ as the total number of
³²⁸ observables.

³²⁹ Collect the RPM and hidden states into a single state vector $\mathbf{y} = [\bar{\mathbf{u}}, \mathbf{w}, \boldsymbol{\beta}]^\top \in \mathbb{R}^{n_y}$, where
³³⁰ $n_y = N + \tilde{N} + m$, and define a data-driven operator $\mathbf{M} \in \mathbb{R}^{n_z \times n_y}$ to define the PIROM's

³³¹ observable as,

$$\mathbf{z} = \mathbf{M}\mathbf{y} \quad (36)$$

³³² where,

$$\mathbf{M} = \begin{bmatrix} \mathbf{M}_{\bar{u}} & \mathbf{0} & \mathbf{M}_{\beta} \\ \mathbf{0} & \mathbf{I} & \mathbf{0} \end{bmatrix} \quad (37)$$

³³³ includes the matrices $\mathbf{M}_{\bar{u}} \in \mathbb{R}^{\tilde{N} \times N}$ and $\mathbf{M}_{\beta} \in \mathbb{R}^{\tilde{N} \times m}$, which computes the surface temperature observable from the RPM states and hidden states, respectively. The PIROM is coupled
³³⁴ to the SVM in eq. (13) by leveraging eq. (36) to compute the surface recession velocity. Thus,
³³⁵ the PIROM is formally stated as,

$$\mathcal{A}\dot{\mathbf{y}} = [\mathcal{B} + \mathcal{C}]\mathbf{y} + \mathcal{F}(t) \quad (38a)$$

$$\mathbf{z} = \mathbf{M}\mathbf{y} \quad (38b)$$

³³⁷ where,

$$\mathcal{A} = \begin{bmatrix} \bar{\mathbf{A}} & \mathbf{O} & \mathbf{O} \\ \mathbf{O} & \mathbf{I} & \mathbf{O} \\ \mathbf{O} & \mathbf{O} & \mathbf{I} \end{bmatrix} \in \mathbb{R}^{n_y \times n_y}, \quad \mathcal{B} = \begin{bmatrix} \bar{\mathbf{B}} & \mathbf{O} & \mathbf{P} \\ \Xi\mathbf{M}_u & \mathbf{O} & \Xi\mathbf{M}_{\beta} \\ \mathbf{Q} & \mathbf{O} & -\Lambda \end{bmatrix} \in \mathbb{R}^{n_y \times n_y}, \quad (39a)$$

$$\mathcal{C} = \begin{bmatrix} \mathbf{O} & \mathbf{O} & \mathbf{D}(\bar{\mathbf{u}}) \\ \mathbf{O} & \mathbf{O} & \mathbf{O} \\ \mathbf{G}(\bar{\mathbf{u}}) & \mathbf{O} & \mathbf{E}(\bar{\mathbf{u}}) \end{bmatrix} \in \mathbb{R}^{n_y \times n_y}, \quad \mathcal{F} = \begin{bmatrix} \bar{\mathbf{f}}(t) \\ -\tilde{\mathbf{f}} \\ \mathbf{R}\bar{\mathbf{f}}(t) \end{bmatrix} \in \mathbb{R}^{n_y} \quad (39b)$$

³³⁸ The learnable parameters in the PIROM are collected as,

$$\Theta = \{\mathbf{P}, \mathbf{Q}, \mathbf{R}, \mathbf{D}(\bar{\mathbf{u}}), \mathbf{G}(\bar{\mathbf{u}}), \mathbf{E}(\bar{\mathbf{u}}), \mathbf{M}_u, \mathbf{M}_{\beta}\}, \in \mathbb{R}^{n_{\theta}} \quad (40)$$

³³⁹ Particularly, the matrices $\mathbf{P}, \mathbf{A}, \mathbf{Q}, \mathbf{R}$ are constants that need to be identified from data, and
³⁴⁰ account for the effects of coarse-graining on the stiffness and forcing matrices. The matrices

³⁴¹ $\mathbf{D}(\bar{\mathbf{u}})$, $\mathbf{E}(\bar{\mathbf{u}})$, $\mathbf{G}(\bar{\mathbf{u}})$ are state-dependent matrices, and account for the effects of coarse-graining
³⁴² on the advection matrix due to mesh motion. Leveraging the DG-FEM formula for the
³⁴³ advection matrix in eq. (55c) in the Appendix, and noting that the ablating velocity in
³⁴⁴ eq. (4) imposes the boundary condition for the mesh motion, the state-dependent matrices
³⁴⁵ for the i -th component are written as,

$$\mathbf{D}(\bar{\mathbf{u}}) \approx \dot{\mathbf{w}}(\bar{\mathbf{u}}) \odot_r \mathbf{D}, \quad \mathbf{G}(\bar{\mathbf{u}}) \approx \mathbf{G} \odot_r \dot{\mathbf{w}}(\bar{\mathbf{u}}), \quad \mathbf{E}(\bar{\mathbf{u}}) \approx \dot{\mathbf{W}}(\bar{\mathbf{u}}) \odot \mathbf{E} \quad (41)$$

³⁴⁶ where $\dot{\mathbf{w}}(\bar{\mathbf{u}})$ is the SVM based on the observable temperature $\bar{\mathbf{u}}$, \odot_r is the row-wise multipli-
³⁴⁷ cation, and $\dot{\mathbf{W}}$ is the concatenation of $\dot{\mathbf{w}}$ for \tilde{m} times, where \tilde{m} corresponds to the number
³⁴⁸ of hidden states per component, i.e., $m = N\tilde{m}$.

³⁴⁹ The PIROM in eq. (38b) incorporates explicit information on the material properties,
³⁵⁰ boundary conditions, and surface recession, and is designed to generalize across parametric
³⁵¹ variations in these inputs. Moreover, the hidden dynamics in eq. (34b) are interpretable,
³⁵² as these retain the functional form of the DG-FEM in eq. (8). The next step is focused on
³⁵³ identifying the unknown data-driven parameters Θ characterizing the hidden dynamics.

³⁵⁴ 3.3 Learning the Hidden Dynamics

³⁵⁵ Learning of the PIROM is achieved through a gradient-based neural-ODE-like approach [3].
³⁵⁶ For ease of presentation, consider the compact form of the PIROM in eq. (38b),

$$\mathcal{D}(\dot{\mathbf{y}}, \mathbf{y}, \boldsymbol{\xi}, \mathcal{F}; \Theta) = \mathbf{0} \quad (42)$$

³⁵⁷ where $\boldsymbol{\xi}$ defines the model parameters, i.e., material properties and B' tables, while \mathcal{F}
³⁵⁸ represents the forcing terms, i.e., the boundary conditions.

³⁵⁹ Consider a dataset of N_s high-fidelity *surface temperature* observable trajectories \mathbf{z}_{HF} ,
³⁶⁰ sampled at p time instances $\{t_k\}_{k=0}^{p-1}$, for different parameter settings $\{\boldsymbol{\xi}^{(l)}\}_{l=1}^{N_s}$ and forcing

³⁶¹ functions $\{\mathcal{F}^{(l)}(t)\}_{l=1}^{N_s}$. The dataset is expressed as,

$$\mathcal{D} = \left\{ \left(t_k, \mathbf{z}_{\text{HF}}^{(l)}(t_k), \boldsymbol{\xi}^{(l)}, \mathcal{F}^{(l)}(t_k) \right) \right\}_{l=1}^{N_s}, \quad k = 0, 1, \dots, p-1 \quad (43)$$

³⁶² In this work, the dataset contains only surface temperature observables – all high-fidelity
³⁶³ information regarding the surface displacements *are assumed to be unavailable during learn-*
³⁶⁴ *ing.*

³⁶⁵ The learning problem is formulated as the following differentially-constrained problem,

$$\min_{\Theta} \quad \mathcal{J}(\Theta; \mathcal{D}) = \sum_{l=1}^{N_s} \int_{t_0}^{t_f} \ell \left(\mathbf{z}_u^{(l)}, \mathbf{z}_{\text{HF}}^{(l)} \right) dt \quad (44a)$$

$$\text{s.t.} \quad \mathbf{0} = \mathcal{D} \left(\dot{\mathbf{y}}^{(l)}, \mathbf{y}^{(l)}, \boldsymbol{\xi}^{(l)}, \mathcal{F}^{(l)}; \Theta \right) \quad (44b)$$

³⁶⁶ for $l = 1, 2, \dots, N_s$, the objective is to minimize the discrepancy between the high-fidelity
³⁶⁷ and PIROM predictions for the l -th trajectory with $\ell \left(\mathbf{z}_u^{(l)}, \mathbf{z}_{\text{HF}}^{(l)} \right) = \left\| \mathbf{z}_u^{(l)} - \mathbf{z}_{\text{HF}}^{(l)} \right\|_2^2$.

³⁶⁸ The gradient-based optimization loop is based on the adjoint variable $\boldsymbol{\lambda}$, governed by the
³⁶⁹ adjoint differential equation,

$$\frac{\partial \ell}{\partial \mathbf{y}} + \boldsymbol{\lambda}^\top \frac{\partial \mathcal{D}}{\partial \mathbf{y}} - \frac{d}{dt} \left(\boldsymbol{\lambda}^\top \frac{\partial \mathcal{D}}{\partial \dot{\mathbf{y}}} \right) = \mathbf{0} \quad (45a)$$

$$\boldsymbol{\lambda}(t_f)^\top \frac{\partial \mathcal{D}}{\partial \dot{\mathbf{y}}(t_f)} = \mathbf{0} \quad (45b)$$

³⁷⁰ Once $\boldsymbol{\lambda}$ is solved, the gradient is computed as,

$$\nabla_{\Theta} \mathcal{J} = \frac{1}{N_s} \sum_{l=1}^{N_s} \int_{t_0}^{t_f} \left(\frac{\partial \ell}{\partial \Theta} + (\boldsymbol{\lambda}^{(l)})^\top \frac{\partial \mathcal{D}}{\partial \Theta} \right) dt \quad (46)$$

³⁷¹

Discussion on TSA?

372 4 Application to Thermal Protection Systems

373 In this section, the proposed PIROM approach is applied to the analysis of thermo-ablative
374 multi-layered hypersonic TPS. The performance of the PIROM is evaluated in terms of
375 *accuracy, generalizability, and computational efficiency*, across a range of boundary condition
376 and surface velocity model parametrizations. The results show PIROM to be a promising
377 candidate for the solution of the impossible trinity of modeling.

378 4.1 Problem Definition

379 Consider the two-dimensional TPS configuration shown in Fig. x with constant material
380 properties within each layer, dimensions, and BCs listed in Table x. Such configuration is
381 representative of the TPS used for the initial concept 3.X vehicle in past studies [8], and in-
382 volves two main layers: an outer ablative layer, and an inner substrate layer. The top ablative
383 layer may be composed of different materials, such as PICA or Avcoat, while the substrate
384 layer is typically made of a high-temperature resistant material, such as carbon-carbon com-
385 posite [6]. The ablative layer, composed of $\tilde{N} = 3$ ablative components, is subjected to
386 strong time-varying and non-uniform heating, while the substrate layer, composed of one
387 non-ablative component, is insulated adiabatically at the outer surface; the total number of
388 components is thus $N = 4$.

389 The lumped-mass representation of the TPS configuration is shown in Fig. 2, where each
390 component Ω_i is represented by a lumped mass with uniform temperature $u_i(t)$. Details
391 regarding the derivation of the LCM for this configuration are provided in Appendix A.
392 The sources of non-linearities studied in this problem originate from the coupling between
393 the thermodynamics and temperature-dependent mesh motion, i.e., geometry-dependent
394 matrices, as well as the heterogeneities across material layers. As shown in Fig. x, perfect
395 thermocouple devices are placed at the surfaces of the ablative layers for the collection of
396 the high-fidelity temperature signals that are used in the following sections for training and

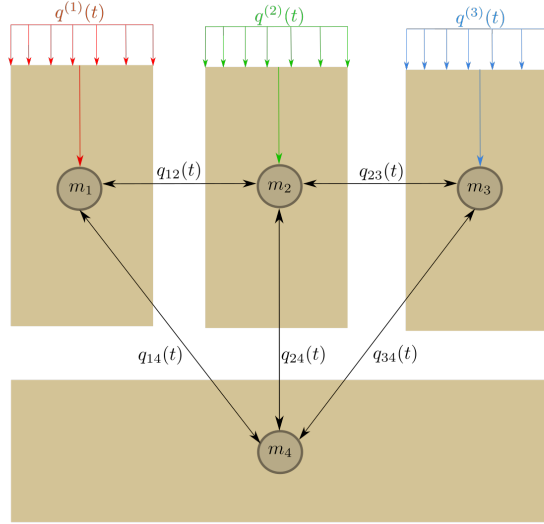


Figure 2: Lumped-mass representation of the multi-layered TPS configuration considered in this work.

³⁹⁷ testing the PIROM.

³⁹⁸ 4.2 Parametrization of Boundary Conditions and Surface Velocity ³⁹⁹ Models

⁴⁰⁰ The operating conditions of the TPS are specified by the boundary conditions, i.e., the heat
⁴⁰¹ flux, and the surface velocity model (SVM). Specifically, the heat flux on the Neumann
⁴⁰² BC is parametrized using $\xi_{\text{BC}} = \{\xi_0, \xi_1, \xi_2\}$, while the SVM is parametrized using $\xi_{\text{SVM}} =$
⁴⁰³ $\{\alpha_1, \alpha_2, \alpha_3\}$. Thus, the heat flux and SVM over the i -th ablative component are expressed
⁴⁰⁴ as,

$$q(x, t; \xi_{\text{BC}}) = \xi_0 e^{\xi_1 x} e^{\xi_2 t}, \forall x \in \Gamma_{i,q}, \quad \dot{w}_i(z_{u,i}; \xi_{\text{SVM}}) = \alpha_i (z_{u,i} - u_{0,i}) \quad (47)$$

⁴⁰⁵ where $\Gamma_{i,q}$, $z_{u,i}$, and $u_{0,i}$ correspond to the Neumann BC surface, the PIROM's surface tem-
⁴⁰⁶ perature prediction, and the initial temperature of the i -th ablative component, respectively.

⁴⁰⁷ The ξ_0 controls the magnitude of the heat flux, while ξ_1 and ξ_2 control the spatial and
⁴⁰⁸ temporal variations, respectively. The constant α_i is a small material-dependent constant
⁴⁰⁹ determined from the B' table, specifying the ablation velocity for a given change in surface

410 temperature.

411 4.3 Data Generation

412 Full-order solutions of the TPS are computed using the FEM multi-mechanics module of
413 the **Aria** package [4], where the mesh is shown in Fig. x. The mesh consists of 2196
414 total elements, with 366 elements for each ablative component and 1098 elements for the
415 substrate component. All solutions are computed for one minute from an uniform initial
416 temperature of $T(x, t_0) = 300$ K. Given an operating condition $\xi = [\xi_{\text{BC}}, \xi_{\text{SVM}}]^{\top}$, a full-
417 order solution consists of then collection of time-varying temperature and displacement fields
418 $\left\{ \left(t_k, \mathbf{u}_{\text{HF}}^{(l)}(t_k), \mathbf{w}_{\text{HF}}^{(l)}(t_k), \xi^{(l)} \right) \right\}_{k=0}^{p-1}$, where p is the number of time steps with a step size of
419 $\Delta t \approx 10^{-3}$. The observable trajectories are representative of near-wall thermocouple sensing
420 of hypersonic flows involving heat transfer. At each time instance t_k , a temperature reading is
421 recorded from each ablative component using the thermocouples shown in Fig. x, resulting
422 in three temperature signals, i.e., the observables $\mathbf{z}_{\text{HF}} \in \mathbb{R}^3$. Therefore, each full-order
423 solution produces one trajectory of observables $\left\{ \left(t_k, \mathbf{z}_{\text{HF}}^{(l)}(t_k), \xi^{(l)} \right) \right\}_{k=0}^{p-1}$. The goal of the
424 PIROM is to predict the surface temperature and displacement as accurately as possible.

425 4.3.1 Definition of Training and Testing Datasets

426 The range of parameters used to generate the training \mathcal{D}_1 and testing $\{\mathcal{D}_2, \mathcal{D}_3\}$ datasets
427 are listed in Table x. The training and testing datasets are designed, respectively, to: (1)
428 minimize the information that the PIROM can “see”, and (2) to maximize the variabil-
429 ity of test operating conditions to examine the PIROM’s generalization performance. A
430 total of 110 normally-distributed data points for the BC parametrization are visualized in
431 Fig. 3(a), and the corresponding observable trajectories are shown in Figs. 3(b) and 3(c).
432 The training dataset \mathcal{D}_1 includes 10 trajectories with randomly selected BC parameters from
433 the 110 points, with nominal SVM parameters $\xi_{\text{SVM}} = \{1, 1, 1\} \times 10^{-6}$. Note that although
434 Fig. 3(c) shows the surface displacements for all ablative components in \mathcal{D}_1 , only the *surface*

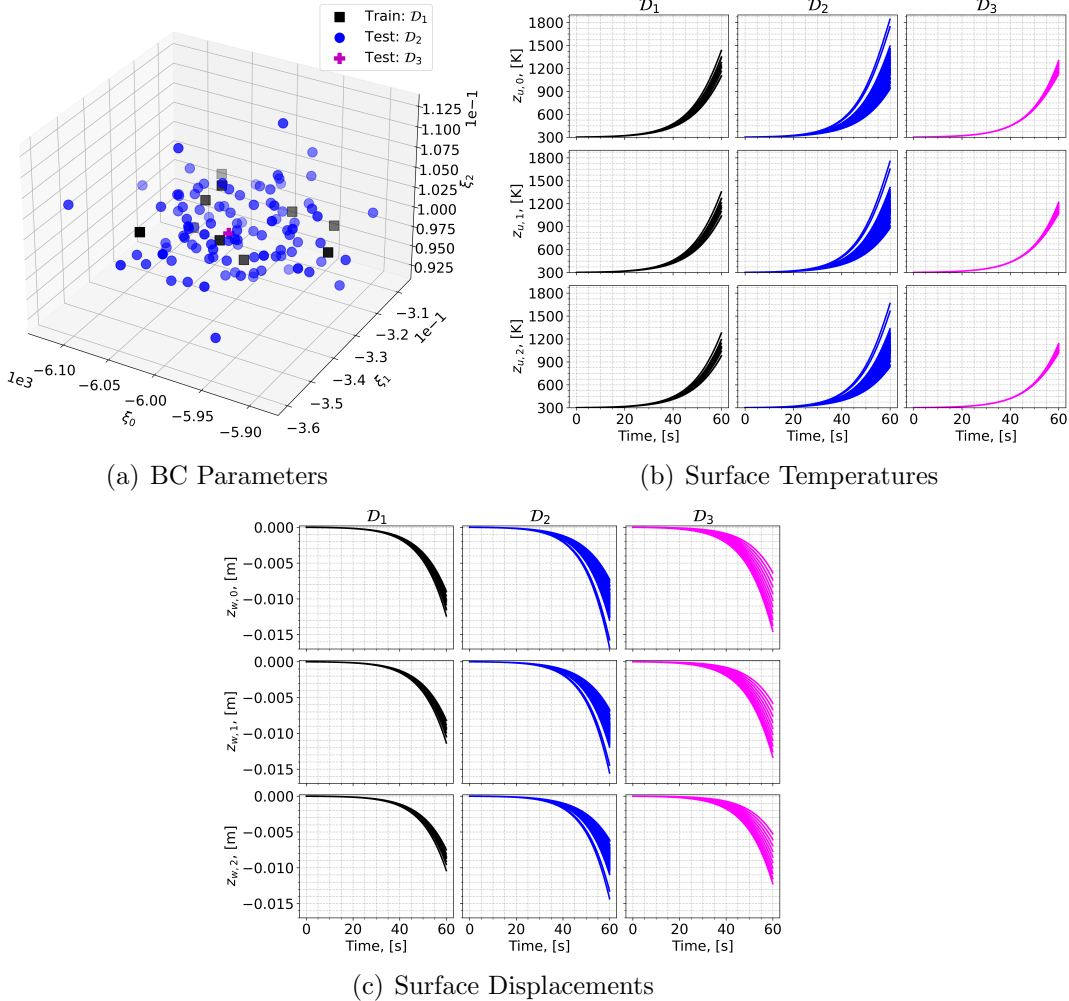


Figure 3: Boundary condition parameters, temperature observables, and displacement observables for the training and testing datasets.

435 *temperature is used for training the PIROM.*

436 Two additional datasets are generated for testing. The dataset \mathcal{D}_2 includes the remaining
 437 100 BC parameter values not considered in \mathcal{D}_1 , and the high-fidelity simulation are generated
 438 with the same nominal SVM parameters. The cases in the \mathcal{D}_3 fixes the boundary condition
 439 as shown in Fig. 3(a) and varies the SVM parameters as shown in Table. **x**. The testing
 440 datasets \mathcal{D}_2 and \mathcal{D}_3 are *out-of-distribution* (OOD) datasets, and are meant for testing the
 441 generalizability of the ROMs to unseen BCs and SVMs, respectively.

442 4.4 Performance Metrics

443 The performance of the PIROM is evaluated by the metrics of prediction error and compu-
 444 tational cost.

445 **Prediction Error** Consider one trajectory of high-fidelity surface temperature and dis-
 446 placement data $\left\{ \left(t_k, \mathbf{z}_{u,\text{HF}}^{(l)}(t_k), \mathbf{z}_{w,\text{HF}}^{(l)}(t_k) \right) \right\}_{k=0}^{p-1}$ for the l -th operating condition in the testing
 447 datasets \mathcal{D}_2 or \mathcal{D}_3 . The difference $e_i^{(l)}$ for the i -th predicted observable, denoted as $z_i^{(l)}$, is
 448 computed as,

$$e_i^{(l)} = \frac{1}{\Delta z_i^{(l)}} \sqrt{\frac{1}{p} \sum_{k=0}^{p-1} \left(z_{i,\text{HF}}^{(l)}(t_k) - z_i^{(l)}(t_k) \right)^2} \quad (48)$$

449 for $i = 1, 2, 3$ and $z_i^{(l)} \in \left\{ z_{i,u}^{(l)}, z_{i,w}^{(l)} \right\}$, and where,

$$\Delta z_i^{(l)} = \max_{0 \leq k \leq p-1} z_{i,\text{HF}}^{(l)}(t_k) - \min_{0 \leq k \leq p-1} z_{i,\text{HF}}^{(l)}(t_k) \quad (49)$$

450 Subsequently, the prediction error of one trajectory is computed by a weighted sum based
 451 on the area of each *ablative component*, resulting in the normalized root mean square error
 452 (NRMSE) metric for one trajectory,

$$\text{NRMSE} = \frac{\sum_{i=1}^{\tilde{N}} |\Omega_i| e_i^{(l)}}{\sum_{i=1}^{\tilde{N}} |\Omega_i|} \times 100\% \quad (50)$$

453 For one dataset, the NRMSE is defined to be the average of the NRMSEs of all trajectories
 454 in the dataset.

455 **Computational Acceleration** The *computational acceleration* metric focuses on the quan-
 456 tification of the speedup factor $\frac{\mathcal{T}_{\text{HF}}(\mathcal{D})}{\mathcal{T}_{\mathcal{M}}(\mathcal{D})}$, where $\mathcal{T}_{\text{HF}}(\mathcal{D})$ and $\mathcal{T}_{\mathcal{M}}(\mathcal{D})$ correspond to the wall-clock
 457 time required by the high-fidelity model and the reduced-order model \mathcal{M} (i.e., PIROM or
 458 RPM) to evaluate all trajectories in the dataset \mathcal{D} , respectively. For a benchmark analysis
 459 of the computational costs during the training phase, please refer to Ref. [12]. All computa-

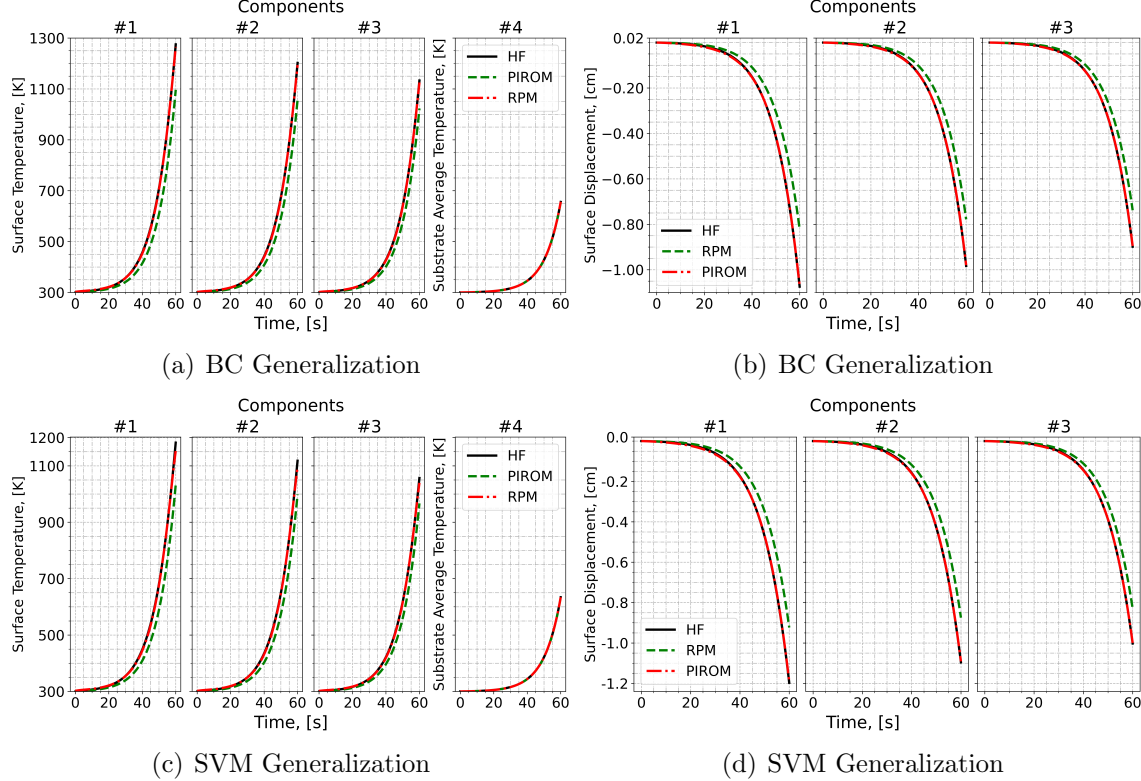


Figure 4: PIROM predictions against high-fidelity solutions for (a)-(b) BC generalization and (c)-(d) SVM generalization.

460 tions are performed in serial for fairness in an Intel Xeon (R) Gold 6258R CPU 2.70GHz
 461 computer with 62 GB of RAM.

462 4.5 Generalization to Boundary Conditions

463 To investigate the generalization performance on the BCs, the PIROM and RPM are tested
 464 using the \mathcal{D}_2 dataset.

465 4.6 Generalization to Surface Velocity Models

466 4.7 Summary of Results

467 5 Conclusions

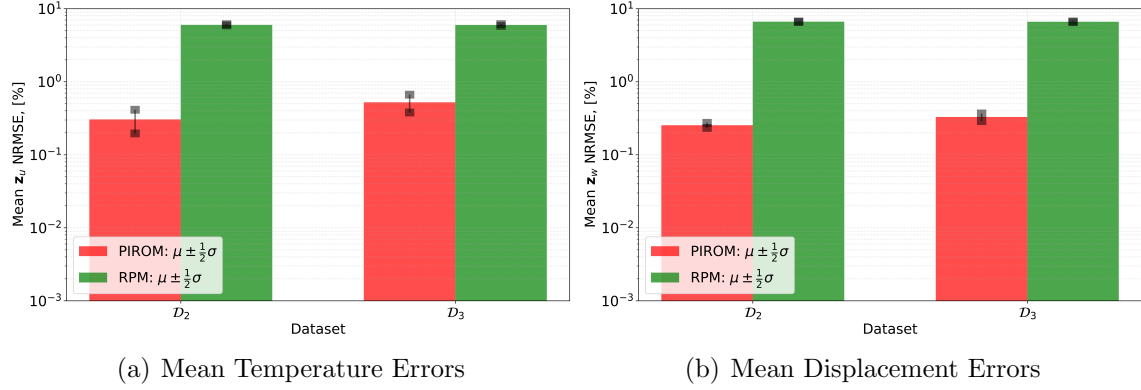


Figure 5: Mean prediction errors for (a) surface temperature and (b) surface displacement across testing datasets.

468 A Technical Details

469 This appendix presents the technical details of the PIROM framework applied to the TPS
 470 ablation problem. The first section provides the mathematical details for the definition of
 471 the DG-FEM. The second section follows the projection procedures from Ref. [x], and demon-
 472 strates the effects of coarse-graining on the advection matrix. The third section presents the
 473 derivation of the LCM model from an energy-conservation perspective.

474 A.1 Full-Order Model

475 To obtain the full-order numerical solution, the governing equation is spatially discretized
 476 using variational principles of Discontinuous Galerkin (DG) to result in a high-dimensional
 477 system of ordinary differential equations (ODEs). The DG-FEM model is written in an
 478 element-wise form, which is beneficial for subsequent derivations of the lower-order models.
 479 Note that the choice of DG approach here is mainly for theoretical convenience in the sub-
 480 sequent coarse-graining formulation. In the numerical results, the full-order TPS ablation
 481 simulations is computed using standard FEM instead, and the equivalence between DG and
 482 standard FEM is noted upon their convergence.

483 **A.1.1 Domain Discretization**

484 Consider a conforming mesh partition of the domain, as shown in Fig. DOMAIN, where each
 485 element belongs to one and only one component. Denote the collection of all M elements
 486 as $\{E_i\}_{i=1}^M$. To ease the description of the DG model, a graph structure is employed. The
 487 elements are treated as vertices, the set of which is denoted $\mathcal{V} = \{m\}_{m=1}^M$. Two neighboring
 488 elements, E_i and E_j , are connected by an edge (i, j) , and the shared boundary between them
 489 is denoted e_{ij} . The collection of all edges are denoted \mathcal{E} , and \mathcal{G} is referred to as a graph.
 490 In the graph, the edges are unidirected, meaning if $(i, j) \in \mathcal{E}$ then $(j, i) \in \mathcal{E}$. Furthermore,
 491 denote the neighbors of the i -th element as $\mathcal{N}_i = \{j | (i, j) \in \mathcal{E}\}$. Lastly, for the ease of
 492 notation, introduce two special indices: T for the boundary of an element that overlaps with
 493 the Dirichlet boundary condition, and similarly q for the Neumann boundary condition.

494 **A.1.2 Weak Form of Discontinuous Galerkin Method**

495 Choosing appropriate basis functions ϕ_k and ϕ_l and using the Interior Penalty Galerkin
 496 (IPG) scheme [5], the variational bilinear form for eq. (1a) is,

$$\sum_{i=1}^M a_{\epsilon,i}(\phi_k, \phi_l) = \sum_{i=1}^M L_i(\phi_k) \quad (51)$$

497 where ϵ is an user-specified parameter and,

$$a_{\epsilon,i}(\phi_k, \phi_l) = \int_{E^{(i)}} \left(\rho c_p \phi_k \frac{\partial \phi_l}{\partial t} + \nabla \phi_k \cdot (\mathbf{k} \nabla \phi_l) - \rho c_p \phi_k \mathbf{v} \cdot \nabla \phi_l \right) dE^{(i)} \quad (52a)$$

$$\begin{aligned} &= - \sum_{j \in \mathcal{N}_i \cup \{T_b\}} \int_{e_{ij}} \{\mathbf{k} \nabla \phi_k \cdot n\} [\phi_l] de_{ij} + \epsilon \sum_{j \in \mathcal{N}_i \cup \{T_b\}} \int_{e_{ij}} \{\mathbf{k} \nabla \phi_l \cdot n\} [\phi_k] de_{ij} \\ &\quad + \sigma \sum_{j \in \mathcal{N}_i \cup \{T_b\}} \int_{e_{ij}} [\phi_k] [\phi_l] de_{ij} \end{aligned} \quad (52b)$$

$$L_i(v) = \epsilon \sum_{j \in \mathcal{N}_i \cup \{T_b\}} \int_{e_{ij}} (\mathbf{k} \nabla \phi_l \cdot n) T_b de_{ij} + \int_{e_{iq}} \phi_k q_b de_{iq} + \sigma \int_{e_{iT}} \phi_k T_b de_{iT} \quad (52c)$$

- ⁴⁹⁸ In the bi-linear form above, the notations $[]$ and $\{\}$ are respectively the jumps and averages
⁴⁹⁹ at the boundary e_{ij} share by two elements E_i and E_j ,

$$[u] = u|_{E_i} - u|_{E_j}, \quad \{u\} = \frac{1}{2} \left(u|_{E_i} + u|_{E_j} \right), \quad \text{for } x \in e_{ij} = E_i \cap E_j$$

⁵⁰⁰ Furthermore, in the bi-linear form, the terms associated with σ are introduced to enforce
⁵⁰¹ the Dirichlet boundary conditions; σ is a penalty factor whose value can depend on the size
⁵⁰² of an element. Depending on the choice of ϵ , the bi-linear form corresponds to symmetric
⁵⁰³ IPG ($\epsilon = -1$), non-symmetric IPG ($\epsilon = 1$), and incomplete IPG ($\epsilon = 0$). All these schemes
⁵⁰⁴ are consistent with the original PDE and have similar convergence rate with respect to mesh
⁵⁰⁵ size. In the following derivations, the case $\epsilon = 0$ is chosen for the sake of simplicity.

⁵⁰⁶ **A.1.3 Discontinuous Galerkin Model**

⁵⁰⁷ Next, the DG-based model is written in an element-wise form. For the i -th element, use a
⁵⁰⁸ set of P trial functions to represent the temperature as in eq. (6). Without loss of generality,
⁵⁰⁹ the trial functions are assumed to be orthogonal, so that $\int_{E^{(i)}} \phi_k^{(i)}(x) \phi_l^{(i)}(x) dx = |E^{(i)}| \delta_{kl}$,
⁵¹⁰ where $|E^{(i)}|$ is the area ($n_d = 2$) or volume ($n_d = 3$) of the i -th element, and δ_{kl} is the
⁵¹¹ Kronecker delta.

⁵¹² Using test functions same as trial functions, the dynamics $\mathbf{u}^{(i)}$ is obtained by evaluating
⁵¹³ the element-wise bi-linear forms,

$$a_{\epsilon,i}(\phi_k^{(i)}, T^{(i)}) = L_i(\phi_k^{(i)}), \quad k = 1, 2, \dots, P \quad (53)$$

⁵¹⁴ The above procedure yields,

$$\mathbf{A}^{(i)} \dot{\mathbf{u}}^{(i)} = (\mathbf{B}^{(i)} + \mathbf{C}^{(i)}(t)) \mathbf{u}^{(i)} + \sum_{j \in \mathcal{N}_i \cup \{T_b\}} \left(\mathbf{B}_{ij}^{(i)} \mathbf{u}^{(i)} + \mathbf{B}_{ij}^{(j)} \mathbf{u}^{(j)} \right) + \mathbf{f}^{(i)}(t) \quad (54)$$

515 where for $k, l = 1, 2, \dots, P$,

$$[\mathbf{A}^{(i)}]_{kl} = \int_{E^{(i)}} \rho c_p \phi_k^{(i)} \phi_l^{(i)} dE^{(i)} \quad (55a)$$

$$[\mathbf{B}^{(i)}]_{kl} = - \int_{E^{(i)}} (\nabla \phi_k^{(i)}) \cdot (\mathbf{k} \nabla \phi_l^{(i)}) dE^{(i)} \quad (55b)$$

$$[\mathbf{C}^{(i)}]_{kl} = \int_{E^{(i)}} \rho c_p \phi_k^{(i)} \mathbf{v}^{(i)} \cdot \nabla \phi_l^{(i)} dE^{(i)} \quad (55c)$$

$$[\mathbf{B}_{ij}^{(i)}] = \int_{e_{ij}} \left\{ \mathbf{k} \nabla \phi_k^{(i)} \cdot \hat{n} \right\} \phi_l^{(i)} - \sigma [\phi_k^{(i)}] \phi_l^{(i)} de_{ij} \quad (55d)$$

$$[\mathbf{B}_{ij}^{(j)}] = \int_{e_{ij}} - \left\{ \mathbf{k} \nabla \phi_k^{(i)} \cdot \hat{n} \right\} \phi_l^{(j)} + \sigma [\phi_k^{(i)}] \phi_l^{(j)} de_{ij} \quad (55e)$$

$$[\mathbf{f}^{(i)}]_k = \int_{e_{iq}} \phi_k^{(i)} q_b de_{iq} + \sigma \int_{e_{iT}} \phi_k^{(i)} de_{iT} \quad (55f)$$

516 The matrices $\mathbf{A}^{(i)} \in \mathbb{R}^{P \times P}$, $\mathbf{B}^{(i)} \in \mathbb{R}^{P \times P}$, and $\mathbf{C}^{(i)} \in \mathbb{R}^{P \times P}$ are respectively the capacitance,
 517 conductivity, and advection matrices for element i . These matrices depend on ρ , c_p , \mathbf{k} , and
 518 \mathbf{v} , and hence can be non-linear functions of $\mathbf{u}^{(i)}$. Since the trial functions are orthogonal, if
 519 ρc_p is constant within an element, $\mathbf{A}^{(i)}$ is diagonal; otherwise, \mathbf{A}_i is symmetric and positive
 520 definite as $\rho c_p > 0$.

521 For compactness, the element-wise model in eq. (54) is also written in matrix form,

$$\mathbf{A}(\dot{\mathbf{u}}) = [\mathbf{B}(\mathbf{u}) + \mathbf{C}(\mathbf{u})] \mathbf{u} + \mathbf{f}(t) \quad (56)$$

522 where $\mathbf{u} = [\mathbf{u}^{(1)}, \mathbf{u}^{(2)}, \dots, \mathbf{u}^{(M)}]^T \in \mathbb{R}^{MP}$ includes all DG variables, $\mathbf{f} = [\mathbf{f}^{(1)}, \mathbf{f}^{(2)}, \dots, \mathbf{f}^{(M)}]^T \in$
 523 \mathbb{R}^{MP} , \mathbf{A} and \mathbf{C} are matrices of M diagonal blocks whose i -th blocks are $\mathbf{A}^{(i)}$ and $\mathbf{C}^{(i)}$, and
 524 \mathbf{B} is a matrix of $M \times M$ blocks whose (i, j) -th block is,

$$\mathbf{B}_{ij} = \begin{cases} \mathbf{B}^{(i)} + \sum_{j \in \mathcal{N}_i \cup \{T_b\}} \mathbf{B}_{ij}^{(i)}, & i = j \\ \mathbf{B}_{ij}^{(j)}, & i \neq j \end{cases} \quad (57)$$

525 The dependency of \mathbf{A} , \mathbf{B} , and \mathbf{C} on \mathbf{u} is explicitly noted in eq. (56), which is the source of

526 non-linearity in the current TPS problem. Moreover, the mesh velocity \mathbf{v} varies with space
527 and time, and thus the advection matrix \mathbf{C} varies with time as a function of q_b .

528 A.2 Coarse-Graining of Dynamics

529 The LCM is obtained by coarse-graining the full-order DG-FEM. This coarse-graining proce-
530 dure produces resolved $\mathbf{r}^{(1)}(\mathbf{u}, t)$ and residual $\mathbf{r}^{(2)}(\mathbf{u}, t)$ dynamics as in eq. (23). This section
531 presents the detail derivations and magnitude analysis for the resolved and residual dynam-
532 ics.

533 A.2.1 Resolved Dynamics

534 Using eq. (20), the resolved dynamics is computed as follows,

$$\mathbf{r}^{(1)}(\mathbf{u}, t) = \mathcal{P} [\Phi^+ \mathbf{A}(\mathbf{u})^{-1} (\mathbf{B}(\mathbf{u})\mathbf{u} + \mathbf{C}(\mathbf{u})\mathbf{u} + \mathbf{f}(t))] \quad (58a)$$

$$\begin{aligned} &= \Phi^+ \mathbf{A}(\mathbf{P}\mathbf{u})^{-1} \mathbf{P}\mathbf{B}(\mathbf{P}\mathbf{u}) \mathbf{P}\mathbf{u} + \Phi^+ \mathbf{A}(\mathbf{P}\mathbf{u})^{-1} \mathbf{P}\mathbf{C}(\mathbf{P}\mathbf{u}) \mathbf{P}\mathbf{u} \\ &\quad + \Phi^+ \mathbf{A}(\mathbf{P}\mathbf{u})^{-1} \mathbf{P}\mathbf{f}(t, \mathbf{P}\mathbf{u}) \end{aligned} \quad (58b)$$

$$\begin{aligned} &= \underbrace{\Phi^+ \mathbf{A}(\Phi\bar{\mathbf{u}})^{-1} \Phi}_{\#1} \underbrace{\Phi^+ \mathbf{B}(\Phi\bar{\mathbf{u}}) \Phi\bar{\mathbf{u}}}_{\#2} + \Phi^+ \mathbf{A}(\Phi\bar{\mathbf{u}})^{-1} \Phi \underbrace{\Phi^+ \mathbf{C}(\Phi\bar{\mathbf{u}}) \Phi\bar{\mathbf{u}}}_{\#3} \\ &\quad + \Phi^+ \mathbf{A}(\Phi\bar{\mathbf{u}})^{-1} \Phi \underbrace{\Phi^+ \mathbf{f}(t, \Phi\bar{\mathbf{u}})}_{\#4} \end{aligned} \quad (58c)$$

535 Detailed derivations for the #1, #2, and #4 terms can be found in Ref. [x](#). The effects of
536 coarse-graining on the advection term #3 are analyzed next.

537 **Term #3** The $\mathbf{C}(\mathbf{u}) \in \mathbb{R}^{MP \times MP}$ matrix contains M diagonal of size $P \times P$, since the
538 basis functions are defined locally on each element. Therefore, $[\mathbf{C}(\mathbf{u})]_{ij} = \mathbf{0}$ for all $i \neq j$ with

⁵³⁹ $i, j = 1, 2, \dots, M$. It follows that for $k, l = 1, 2, \dots, N$,

$$[\Phi^+ \mathbf{C}(t, \Phi \bar{\mathbf{u}}) \Phi]_{kl} = \sum_{i=1}^M \sum_{j=1}^M \boldsymbol{\varphi}_i^{k+} [\mathbf{C}(t, \Phi \bar{\mathbf{u}})]_{ij} \boldsymbol{\varphi}_j^l \quad (59a)$$

$$= \sum_{i=1}^M \boldsymbol{\varphi}_i^{k+} [\mathbf{C}(t, \Phi \bar{\mathbf{u}})]_{ii} \boldsymbol{\varphi}_i^l \quad (59b)$$

$$= \sum_{i \in \mathcal{V}_k} \boldsymbol{\varphi}_i^{k+} [\mathbf{C}(t, \Phi \bar{\mathbf{u}})]_{ii} \boldsymbol{\varphi}_i^l \quad (59c)$$

⁵⁴⁰ where in the second row, the fact that $[\mathbf{C}(\mathbf{u})]_{ij} = 0$ for all $i \neq j$ is used, and in the last row,
⁵⁴¹ the fact that $\boldsymbol{\varphi}_i^{k+} = 0$ for all $i \notin \mathcal{V}_k$ is used. Now, considering that $[\mathbf{C}(\mathbf{u})]_{ii}$ has a $(1, 1)$ -th
⁵⁴² zero element, i.e., $[C_{11}(t, \Phi \bar{\mathbf{u}})]_{ii} = 0$, and that if $k \neq l$ then $i \notin \mathcal{V}_l$ and thus $\boldsymbol{\varphi}_i^l = \mathbf{0}$, it follows
⁵⁴³ that for some index $i \in \mathcal{V}_k$,

$$\boldsymbol{\varphi}_i^{k+} [\mathbf{C}(t, \Phi \bar{\mathbf{u}})]_{ii} \boldsymbol{\varphi}_i^l = \boldsymbol{\varphi}_i^{k+} [\mathbf{C}(t, \Phi \bar{\mathbf{u}})]_{ii} \boldsymbol{\varphi}_i^k = \frac{|E_i|}{|\Omega_k|} [C_{11}(t, \Phi \bar{\mathbf{u}})]_{ii} = 0 \quad (60)$$

⁵⁴⁴ The matrix $[\Phi^+ \mathbf{C}(t, \Phi \bar{\mathbf{u}}) \Phi]_{kl} = 0$ for all $k, l = 1, 2, \dots, N$, and thus,

$$\bar{\mathbf{C}}(t, \bar{\mathbf{u}}) = \Phi^+ \mathbf{C}(t, \Phi \bar{\mathbf{u}}) \Phi = \mathbf{0} \quad (61)$$

⁵⁴⁵ as indicated by the LCM in eq. (9).

546 **A.2.2 Magnitude Analysis for Residual Dynamics**

547 Next, the magnitude of the residual dynamics $\mathbf{r}^{(2)}(\mathbf{u}, t)$ is analyzed to pinpoint the missing
 548 physics in the LCM. By definition,

$$\mathbf{r}^{(2)}(\mathbf{u}, t) = \dot{\bar{\mathbf{u}}} - \mathbf{r}^{(1)}(\bar{\mathbf{u}}, t) \quad (62a)$$

$$= \Phi^+ \mathbf{r}(\mathbf{u}, t) - \mathbf{r}^{(1)}(\mathbf{u}, t) \quad (62b)$$

$$\begin{aligned} &= \underbrace{\Phi^+ \mathbf{A}(\mathbf{u})^{-1} \mathbf{B}(\mathbf{u}) \mathbf{u} - \bar{\mathbf{A}}(\bar{\mathbf{u}})^{-1} \bar{\mathbf{B}}(\bar{\mathbf{u}}) \bar{\mathbf{u}}}_{\#1} + \underbrace{\Phi^+ \mathbf{A}(\mathbf{u})^{-1} \mathbf{C}(\mathbf{u}) \mathbf{u} - \bar{\mathbf{A}}(\bar{\mathbf{u}})^{-1} \bar{\mathbf{C}}(t, \bar{\mathbf{u}}) \bar{\mathbf{u}}}_{\#2} \\ &\quad + \underbrace{\Phi^+ \mathbf{A}(\mathbf{u})^{-1} \mathbf{f}(t) - \bar{\mathbf{A}}(\bar{\mathbf{u}})^{-1} \bar{\mathbf{f}}(t)}_{\#3} \end{aligned} \quad (62c)$$

549 The magnitude analysis for terms #1 and #3 can be found in Ref. [x]. The analysis for term
 550 #2 is presented next. Let $\mathbf{D}(\bar{\mathbf{u}}) = \mathbf{A}(\Phi \bar{\mathbf{u}})^{-1} \mathbf{P} \mathbf{C}(t, \Phi \bar{\mathbf{u}})$, then,

$$\Phi^+ \mathbf{A}(\mathbf{u})^{-1} \mathbf{C}(\mathbf{u}) \mathbf{u} - \bar{\mathbf{A}}(\bar{\mathbf{u}})^{-1} \bar{\mathbf{C}}(t, \bar{\mathbf{u}}) \bar{\mathbf{u}} \quad (63a)$$

$$= \Phi^+ \mathbf{A}(\mathbf{u})^{-1} \mathbf{C}(\mathbf{u}) \mathbf{u} - \Phi^+ \mathbf{A}(\Phi \bar{\mathbf{u}})^{-1} \mathbf{P} \mathbf{C}(t, \Phi \bar{\mathbf{u}}) \Phi \Phi^+ \mathbf{u} \quad (63b)$$

$$= \Phi^+ \mathbf{A}^{-1}(\mathbf{u}) \mathbf{C}(\mathbf{u}) \mathbf{u} - \Phi^+ \mathbf{D}(\bar{\mathbf{u}}) \Phi \Phi^+ \mathbf{u} \quad (63c)$$

$$(63d)$$

551 where $\mathbf{P} = \Phi \Phi^+$. Thus,

$$\|\Phi^+ \mathbf{A}(\mathbf{u})^{-1} \mathbf{C}(\mathbf{u}) \mathbf{u} - \bar{\mathbf{A}}^{-1}(\bar{\mathbf{u}}) \bar{\mathbf{C}}(t, \bar{\mathbf{u}}) \bar{\mathbf{u}}\| \quad (64a)$$

$$\leq \|\Phi^+ \mathbf{A}^{-1}(\mathbf{u}) \mathbf{C}(\mathbf{u}) \mathbf{u} - \Phi^+ \mathbf{D}(\bar{\mathbf{u}}) \mathbf{u}\| + \|\Phi^+ \mathbf{D}(\bar{\mathbf{u}}) \mathbf{u} - \Phi^+ \mathbf{D}(\bar{\mathbf{u}}) \Phi \Phi^+ \mathbf{u}\| \quad (64b)$$

$$\leq \|\Phi^+\| \underbrace{\|\mathbf{A}^{-1}(\mathbf{u}) \mathbf{C}(\mathbf{u}) \mathbf{u} - \mathbf{D}(\bar{\mathbf{u}}) \mathbf{u}\|}_{\#1} + \|\Phi^+ \mathbf{D}(\bar{\mathbf{u}})\| \underbrace{\|\mathbf{u} - \Phi \Phi^+ \mathbf{u}\|}_{\#2} \quad (64c)$$

552 where term #2 is due to the approximation of non-uniform temperature as constants, and
 553 term #1 is the error in the advection dynamics due to coarse-graining.

554 A.3 Lumped Capacitance Model

555 The following assumptions are employed: (1) the temperature in component (i) is described
 556 by a scalar time-varying average temperature $\bar{u}^{(i)}$, (2) between neighboring components (i)
 557 and (j) the heat flux is approximated as,

$$q_{ij} = \frac{\bar{u}^{(j)} - \bar{u}^{(i)}}{R_{ij}} \quad (65)$$

558 where R_{ij} is the thermal resistance. Empirically, for a component of isotropic heat conduc-
 559 tivity k , length ℓ , and cross-section area A , the thermal resistance is $R = \ell/kA$. Between
 560 components i and j , define $R_{ij} = R_i + R_j$. In addition, the heat flux due to Dirichlet
 561 boundary condition is computed as $q_{iT} = (T_b - \bar{u}^{(i)})/R_i$.

562 At component i , the dynamics of LCM are given by,

$$\int_{E^{(i)}} \rho c_p \dot{\bar{u}}^{(i)} dE^{(i)} = \left(\sum_{j \in \mathcal{N}_i} \int_{e_{ij}} \frac{\bar{u}^{(j)} - \bar{u}^{(i)}}{R_{ij}} de_{ij} \right) + \int_{e_{iq}} q_b de_{iq} + \int_{e_{iT}} \frac{T_b - \bar{u}^{(i)}}{R_i} de_{iT} \quad (66a)$$

$$\bar{A}^{(i)} \dot{\bar{u}}^{(i)} = \left(\sum_{j \in \mathcal{N}_i} \frac{|e_{ij}|}{R_{ij}} (\bar{u}^{(j)} - \bar{u}^{(i)}) \right) + |e_{iq}| \bar{q}^{(i)} + \frac{|e_{iT}|}{R_i} (\bar{T}^{(i)} - \bar{u}^{(i)}) \quad (66b)$$

$$= \sum_{j \in \mathcal{N}_i} \left(-\frac{|e_{ij}|}{R_{ij}} \bar{u}^{(i)} + \frac{|e_{ij}|}{R_{ij}} \bar{u}^{(j)} \right) + \left(-\frac{|e_{iT}|}{R_i} \bar{u}^{(i)} \right) + \left(|e_{iq}| \bar{q}^{(i)} + \frac{|e_{iT}|}{R_i} \bar{T}^{(i)} \right) \quad (66c)$$

$$= \sum_{j \in \mathcal{N}_i \cup \{T_b\}} \left(\bar{B}_{ij}^{(i)} \bar{u}^{(i)} + \bar{B}_{ij}^{(j)} \bar{u}^{(j)} \right) + \bar{f}^{(i)} \quad (66d)$$

563 where in eq. (66b) $|e|$ denotes the length ($d = 2$) or area ($d = 3$) of a component boundary
 564 e . The $\bar{A}^{(i)}$, $\bar{B}_{ij}^{(i)}$, and $\bar{B}_{ij}^{(j)}$ quantities are provided in eq. (12).

565 The lumped-mass representation for the four-component TPS is shown in Fig. ???. Let
 566 v_i represent the area of the i -th element, $\rho c_{p,i}$, the heat capacity evaluated using the average
 567 temperature $\bar{u}^{(i)}$, and $1/R_{ij} = 1/R_i(\bar{u}^{(i)}) + 1/R_j(\bar{u}^{(j)})$ the equivalent thermal resistance
 568 between elements i and j . Leveraging the formulas from eqs. (11b) and (12), the LCM

569 matrices are given by,

$$\bar{\mathbf{A}} = \begin{bmatrix} \overline{\rho c_p}_1 v_1 & 0 & 0 & 0 \\ 0 & \overline{\rho c_p}_2 v_2 & 0 & 0 \\ 0 & 0 & \overline{\rho c_p}_3 v_3 & 0 \\ 0 & 0 & 0 & \overline{\rho c_p}_4 v_4 \end{bmatrix}, \quad (67a)$$

$$\bar{\mathbf{B}} = \begin{bmatrix} \frac{1}{R_{12}} + \frac{1}{R_{14}} & -\frac{1}{R_{12}} & 0 & -\frac{1}{R_{14}} \\ -\frac{1}{R_{12}} & \frac{1}{R_{12}} + \frac{1}{R_{24}} + \frac{1}{R_{23}} & -\frac{1}{R_{23}} & -\frac{1}{R_{24}} \\ 0 & -\frac{1}{R_{32}} & \frac{1}{R_{32}} + \frac{1}{R_{34}} & -\frac{1}{R_{34}} \\ -\frac{1}{R_{14}} & -\frac{1}{R_{24}} & -\frac{1}{R_{34}} & \frac{1}{R_{14}} + \frac{1}{R_{24}} + \frac{1}{R_{34}} \end{bmatrix}, \quad \bar{\mathbf{f}} = \begin{bmatrix} \bar{q}^{(1)} \\ \bar{q}^{(2)} \\ \bar{q}^{(3)} \\ 0 \end{bmatrix} \quad (67b)$$

570 References

- 571 [1] Adam J. Amar, A. Brandon Oliver, Benjamin S. Kirk, Giovanni Salazar, and Justin
Droba. Overview of the charring ablator response (char) code. In AIAA, editor, *AIAA
572 Aviation Forum*, 2016.
- 573 [2] Guy L. Bergel, Frank B. Beckwith, Gabriel J. de Frias, Kevin M. Manktelow, Mark T.
Merewether, Scott T. Miller, Krishen J. Parmar, Timothy S. Shelton, Jesse T. Thomas,
574 Jeremy T. Trageser, Benjamin T. Treweek, Michael V. Veilleux, and Ellen B. Wagman.
Sierra/SolidMechanics 5.6 User's Manual, 2022.
- 575 [3] Ricky T. Q. Chen, Yulia Rubanova, Jesse Bettencourt, and David Duvenaud. Neural
ordinary differential equations, 2019.
- 576 [4] Jonathan Clausen, Victor Brunini, Lincoln Collins, Robert C Knaus, Alec Kucala,
Stephen Lin, Daniel Robert Moser, Malachi Phillips, Thomas Michael Ransegrenola,
Samuel Ramirez Subia, et al. Sierra multimechanics module: Aria verification manual-
577 version 5.22. Technical report, Sandia National Lab.(SNL-NM), Albuquerque, NM
(United States), 2024.

- 585 [5] Gary Cohen and Sebastien Pernet. *Finite Element and Discontinuous Galerkin Methods*
586 for Transient Wave Equations. Springer Dordrecht, Le Chesnay and Toulouse France,
587 2018.
- 588 [6] Matthew Gasch, Keith Peterson, Mairead Stackpoole, Ethiraj Venkatapathy, Gregory
589 Gonzales, and Kyle Hendrickson. Development of advanced ablative carbon phenolic
590 tps for future nasa missions and commercial space. In *38th Annual Small Satellite*
591 *Conference*, Logan, Utah, May 2024.
- 592 [7] Frank P. Incropera, David P. DeWitt, Theodore L. Bergman, and Adrienne S. Lavine.
593 *Fundamentals of Heat and Mass Transfer*. Wiley, Hoboken, NJ, 7th edition, 2011.
- 594 [8] R. J. Klock and Carlos Cesnik. Nonlinear thermal reduced-order modeling for hypersonic
595 vehicles. *AIAA Journal*, 55(7), 2017.
- 596 [9] Eric Parish and Karthik Duraisamy. Non-markovian closure models for large eddy
597 simulations using the mori-zwanzig formalism. *Phys. Rev. Fluids*, 2:014604, Jan 2017.
- 598 [10] Eric Parish and Karthik Duraisamy. A unified framework for multiscale modeling using
599 the mori-zwanzig formalism and the variational multiscale method. *ArXiv*, 12 2017.
- 600 [11] Eric Parish and Karthik Duraisamy. *Coarse-Graining Turbulence Using the*
601 *Mori-Zwanzig Formalism*. Cambridge University Press, Cambridge, 2025.
- 602 [12] Carlos A. Vargas Venegas, Daning Huang, Patrick Blonigan, and John Tencer. Physics-
603 infused reduced-order modeling for analysis of multi-layered hypersonic thermal protec-
604 tion systems. *ArXiv*, 2025.
- 605 [13] Yin Yu, John Harlim, Daning Huang, and Yan Li. Learning coarse-grained dynamics
606 on graph. *arXiv preprint arXiv:2405.09324*, 2024.